Supplementary Information - Current Induced Hidden States in Josephson Junctions

Shaowen Chen[1†*], Seunghyun Park[1†], Uri Vool[1,2], Nikola Maksimovic[1], David A. Broadway[3], Mykhailo Flaks[3], Tony X. Zhou[1‡], Patrick Maletinsky[3], Ady Stern[4], Bertrand I. Halperin[1], and Amir Yacoby[1*]

[1] *Department of Physics, Harvard University, Cambridge MA, 02138, USA*

[2] *Max Planck Institute for Chemical Physics of Solids, 01187 Dresden, Germany*

[3] *Department of Physics, University of Basel, Klingelbergstrasse 82, Basel CH-4056, Switzerland*

[4] *Weizmann Institute of Science, Rehovot, 76100, Israel*

[†] *These authors contributed equally to this work,*

[*] *shaowenchen@g.harvard.edu (S.C.); yacoby@g.harvard.edu (A.Y.) and*

[‡] *Present address: Northrop Grumman Mission Systems, Linthicum MD, 21090, USA*

Supplementary Note 1. PENETRATION LENGTH MEASURED BY NV MAGNETOMETRY

In this section, we measure the Meissner screening of NbN electrodes with NV magnetometry and extract the penetration length. We utilize a NV control sequence that only has the $\frac{\pi}{2}$-pulses at the start and the end (Ramsey sequence), which directly measures the Meissner field generated by the SC, projected along the NV axis. The measurements are done at external magnetic field $B_z = 0.5$ mT where no vortex is present in either the JJ or the SC. The bias current is zero. We show the z-component of the Meissner field around the junction at 4K (Supplementary Fig. 1a), and 7K (Supplementary Fig. 1c). Stronger screening can be seen at 4K compared with 7K, indicating a shorter penetration length.

To extract the absolute value of the Pearl length λ_p, the Meissner field b_z is fit by numerically solving the 1D London equation, which applies a SC strip that is narrow in the x-direction and long in the y-direction [1]. The total magnetic field consists of the external field $B_{z,ext}$, and the Meissner screening field. Using the second London equation,

$$B_{z,ext} + \frac{\mu_0}{2\pi}\int_{-\frac{L}{2}}^{\frac{L}{2}} \frac{J_y(x')}{x'-x}\,dx' = -\mu_0\lambda_p\frac{\partial J_y(x)}{\partial x} \tag{1}$$

where $\lambda_p = \lambda_L^2/t$ is the pearl length, λ_L is the London penetration length, t is thickness of NbN, $J_y(x)$ is the Meissner sheet current of the NbN film, μ_0 is the vacuum permeability. The integral equation is solved by discretizing the variables, and the Meissner field is compared with the measurement. We take a line cut of b_z at about 500 nm away from normal metal area, to avoid influence from the Josephson current. The b_z is fit with Supplementary Supplementary Eqn. 1 to extract λ_p, using $B_{z,ext} = 0.5$ mT, $L = 1.5$ μm. We find $\lambda_p = 4.7 \pm 0.4\mu$m at 4 K (Supplementary Fig. 1b), and 13.7 $\pm$ 1.4 μm at 7 K (Supplementary Fig. 1d). The corresponding London penetration length is $\lambda_L = 410\pm$ 20 nm at 4 K and 690 $\pm$ 35 nm at 7 K. In comparison, previous indirect measurements of λ_p range from 1 to 5 μm at 4 K [2–5].

With these results we can calculate the Josephson penetration length, $\lambda_J = \sqrt{\frac{\Phi_0 L t}{4\pi\mu_0 J_c \lambda_L^2}}$. In our device, $L = 1.5$ μm, thickness $t = 35$ nm, assuming uniform $J_c = I_c/L$ at zero magnetic field, we find $\lambda_J = 780 \pm 40$ nm at $T = 4$ K, and $\lambda_J = 1470 \pm 75$ nm at $T = 7$ K.

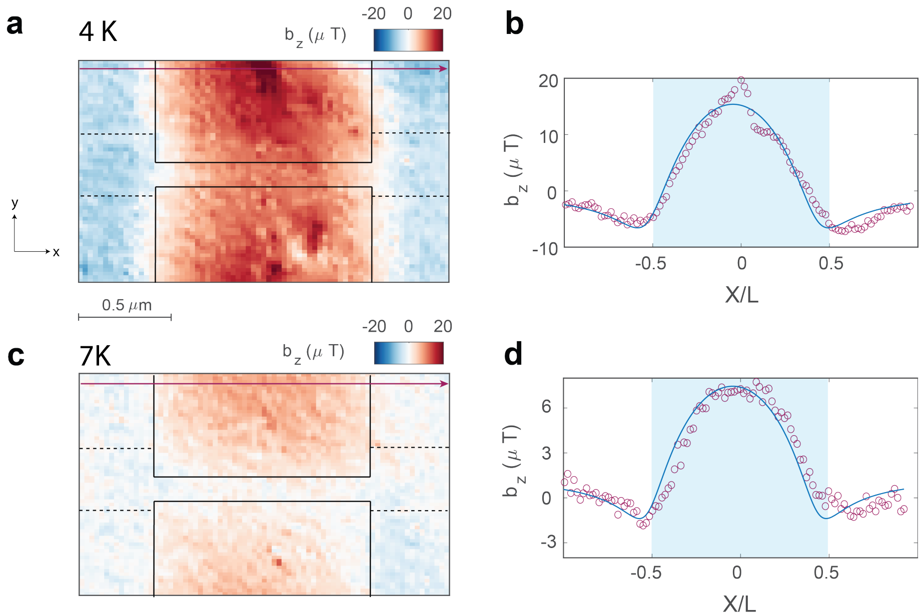

Supplementary Figure 1. **Penetration length measured with NV magnetometry.** **a,** z-component of the Meissner screening field b_z over the JJ and the SC electrodes. The measurement is done at external field $B_z = 0.5$ mT, and $T = 4$ K. The solid lines indicate SC electrodes and the dashed line is the normal metal. **b,** Circles show the measured Meissner field b_z along the red line in (A), which is far away from the junction region. The line is the calculated magnetic field b_z at the NV, generated by the Meissner current using Biot-Savart law. The Meissner current is obtained using the fitting result of λ_p and Supplementary Eqn. 1. Blue shaded area indicate the extent of the SC electrode. The kink in b_z near $x = 0$ is a measurement artifact. **c-d,** are similar results as **a-b**, but measured at $T = 7$ K.

Supplementary Note 2. EVOLUTION OF JOSEPHSON CURRENT FLOW WITH EXTERNAL MAGNETIC FIELD IN WEAK JUNCTIONS

In this section, we evaluate how external magnetic field B_z contributes to the evolution of Josephson current flow and JVs. As discussed in the main text, B_z affects $\phi_e(x)$, the profile of the super current, and modify the number of vortices trapped inside the junction. In the thin film, 1-D line junction ($W \ll L$), and weak junction limit, $\phi_e(x) \propto B_z \cdot \sigma(x)$, where $\sigma(x)$ is a non-linear function shown in Supplementary Eqn. 9 [6].

Here, we simplify $\sigma(x)$ to a linear function to more intuitively show the magnetic field effect, $\phi_e(x) = 2\pi \frac{\Phi_z}{\Phi_0} \frac{x}{L}$. $\Phi_z = B_z \cdot A$ is the magnetic flux through the junction, A is the junction area. This applies to JJs made with bulk superconductors. Nevertheless it still captures the changes of the Josephson current flow with B_z. In this model, when B_z reaches the critical current nodes $\Phi_z = n\Phi_0$, the n-th JV enters the JJ (Supplementary Fig. 2b).

Consider the Gibbs free energy of the junction without external bias current,

$$G(\phi_{\text{bias}}) = \frac{\Phi_0}{2\pi} \cdot [I_c(\Phi_z)(1 - \cos\phi_{\text{bias}})] \tag{2}$$

$I_c(\Phi_z)$ is the critical current when the external magnetic flux is Φ_z, which changes sign at $\Phi_z = n\Phi_0$ (see Supplementary Eqn. 3 and accompanying text). As a result, the ϕ_{bias} which corresponds to the free energy minimum shifts by π, and the local current density, $\propto \sin[\phi_e(x) + \phi_{\text{bias}}]$ changes sign when a Josephson vortex enters/exits the junction.

The periodicity of the oscillating Josephson current $J_y(x)$ shrinks with increasing Φ_z, as seen by the current profile at the critical current (Supplementary Fig. 2c, e), and at zero bias current (Supplementary Fig. 2d, f). The $J_y(x)$ profile changes sign as Φ_z crosses the node from $0.99\Phi_0$ to $1.01\Phi_0$, and around every $n\Phi_0$ thereafter (Supplementary Fig. 2d, f).

We note that in the thin film limit and weak junctions, the JVs enter the junction at critical current nodes B_n as mentioned in the main text. But at the nodes, the magnetic flux through the effective area $A_{\text{eff}} = L^2/1.842$, $B_n \cdot A_{\text{eff}}$ is not exactly $n\Phi_0$ [6]. For example, at B_0 the magnetic flux through the effective area is 0.8173 Φ_0, as shown in Supplementary Table 1. Nevertheless, the $J_y(x)$ periodicity and sign changes with B_z still apply.

In summary, external magnetic flux manipulates Josephson current flow by changing the current profile and the number of JV, making it an important control knob in engineering SC devices.

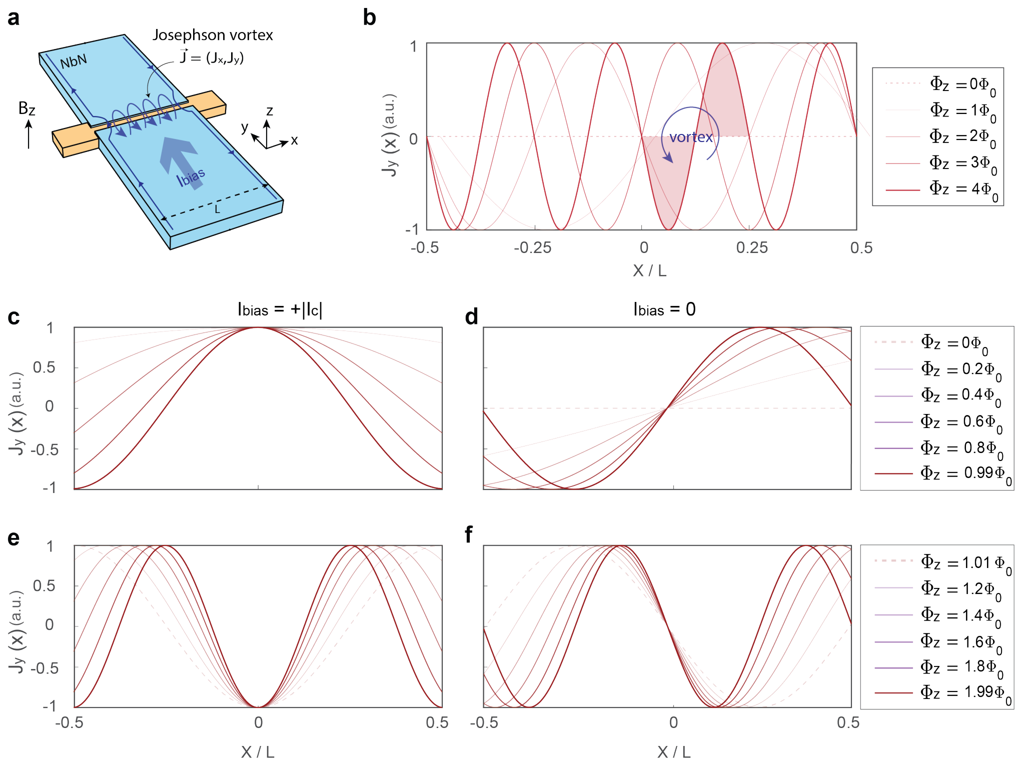

Supplementary Figure 2. **Evolution of Josephson current profile with external magnetic flux.** **a,** Schematics of Josephson current flow for $\Phi_z = 4\Phi_0$. Blue arrows on the device is how the current flows for $I_{\text{bias}} = 0$. **b,** Line cut of J_y at the junction with various fields from zero-flux to $\Phi_z = 4\Phi_0$. Shaded area indicates a JV. **c,e** $I_{\text{bias}} = +|I_c|$ and **d,f** $I_{\text{bias}} = 0$ current flow in different magnetic flux. **c-d** is flux between 0 to $1\Phi_0$ and **e-f** is flux between 1 to $2\Phi_0$.

Supplementary Note 3. JOSEPHSON CURRENT FLOW AND SC PHASE DIFFERENCE ϕ_{bias} AT FINITE MAGNETIC FLUX

In this section, we derive how the bias current I_{bias} controls the phase difference between SC electrodes ϕ_{bias}, at a finite external magnetic field B_z. We show (i) the bias current - ϕ_{bias} relation at finite B_z and (ii) the π phase shift associated with each JV in the junction.

We consider the junction spans between $x \in [-\frac{L}{2}, \frac{L}{2}]$, so ϕ_{bias} is the phase difference between SC electrodes at $x = 0$. We assume the critical current density is constant J_c, and start with the simplified case, $\phi_e(x) = 2\pi\frac{\Phi_z}{\Phi_0}\frac{x}{L}$. $\Phi_z = B_z \cdot A$ is the magnetic flux through the junction, A is the junction area. This applies to JJs made with bulk superconductors. The external bias current is

$$I_{\text{bias}} = \int_{-L/2}^{L/2} J(x)\,dx = \int_{-L/2}^{L/2} J_c \sin\left(2\pi\frac{\Phi_z}{\Phi_0}\frac{x}{L} + \phi_{\text{bias}}\right) dx = J_c L \operatorname{sinc}\left(\pi\frac{\Phi_z}{\Phi_0}\right)\cdot \sin\phi_{\text{bias}} \tag{3}$$

This shows the sinusoidal current-phase relation still applies at finite field. Here $I_c(\Phi_z) = J_c L \cdot \operatorname{sinc}\left(\pi\frac{\Phi_z}{\Phi_0}\right)$ is the critical current at finite flux Φ_z. As a result, ϕ_{bias} can be controlled by I_{bias} via

$$\phi_{\text{bias}} = \arcsin\left(\frac{I_{\text{bias}}}{I_c(\Phi_z)}\right) + n\pi \tag{4}$$

where n is the number of JV, which shifts the phase difference by $n\pi$. Intuitively, each JV has 2π phase winding around itself and this leads to π phase difference at the center of the junction $x = 0$.

The phase shift due to JV can also be understood from an effective Gibbs free energy of the junction. The bias current adds a term to Eq. (2), giving

$$G = \frac{\Phi_z}{2\pi}\cdot\left[I_c(\Phi_z)(1-\cos\phi_{\text{bias}}) - I_{\text{bias}}\phi_{\text{bias}}\right] \tag{5}$$

This is the well known “washboard” potential for biased JJ, and for the over-damped junction, the equilibrium ϕ_{bias} occurs at the local minima of the free energy ($\frac{\partial G}{\partial\phi_{\text{bias}}} = 0$ and $\frac{\partial^2 G}{\partial\phi_{\text{bias}}^2} > 0$). For odd number of JV at the junction, $I_c(\Phi_z) < 0$, which leads to the π phase shift when JV enters or exits the junction.

In the thin film weak-junction limit, $\phi_e(x)$ is given by Supplementary Eqn. 9. The total current is then given by

$$\begin{aligned} I_{\text{bias}} &= \operatorname{Im}\int_{-L/2}^{L/2} J_c(x)e^{i[\phi_{e0}\sigma(x)+\phi_{\text{bias}}]}\,dx \\ &\equiv I_c(B_z)\,\sin[\phi_{\text{bias}}+\phi_c] \end{aligned} \tag{6}$$

where

$$I_c(B_z) = \left|\int_{-L/2}^{L/2} J_c(x)e^{i\phi_{e0}\sigma(x)}\,dx\right|, \tag{7}$$

$$\phi_c = \arg\left(\int_{-L/2}^{L/2} J_c(x)e^{i\phi_{e0}\sigma(x)}\,dx\right). \tag{8}$$

Equation 4 can still apply in the thin film limit. We see that in the weak-junction limit, the dependence of the current on phase remains sinusoidal even if J_c depends on x. In particular, when J_c is a constant, $\phi_c = 0$, and the current phase relation in Supplementary Eqn. 4 can apply.

Supplementary Note 4. THIN FILM JOSEPHSON JUNCTION AND EXTRACTING $\Delta\phi$, ϕ_{eff}

In this section we show (i) transport evidence of the junction being in the thin film limit, and (ii) the fitting methods to extract $\Delta\phi$ and ϕ_{eff} shown in Fig. 2d, h in the main text.

i. Thin film SC In a junction with $W \ll L$, $\phi_e(x)$ can be derived from the x-direction screening currents in the thin film SC leads, treated as semi-infinite strips with the boundary condition of zero Josephson current, $J_y(x) = 0$ at $y = 0$ (center of the junction). We assume the external contact electrodes are located at positions $y = \pm H$, with $H \gg L$. To leading order all screening currents flow within the SC electrodes and hence the boundary condition. One then finds, following Ref. [6, 7]

$$\begin{aligned} \phi_e(x, B_z) &= \frac{16 B_z L^2}{\pi^2 \Phi_0} \cdot \sigma(\pi x/L) \equiv \phi_{e0} \cdot \sigma(\pi x/L), \\ \sigma(\zeta) &= \sum_{n=0}^{n=\infty} (-1)^n \frac{\sin{(2n+1)\zeta}}{(2n+1)^3} \end{aligned} \tag{9}$$

where Φ_0 is the flux quantum. $\sigma(\zeta)$ is an odd function of its argument and may be reasonably approximated by $\sigma(\zeta) \approx \sin\zeta$. The scale of ϕ_e is set by the quantity $\phi_{e0} \equiv \phi_e|_{x=L/2} \approx 1.7 B_z L^2/\Phi_0$. In this model, the $\phi_e(x)$ is induced by the screening current in the SC electrodes. Its shape is determined by the $\sigma(\zeta)$ function and its amplitude ϕ_{e0}, is proportional to the magnetic field B_z. As mentioned in the main text, this model does not include the Josephson current induced phase in strong junctions.

Ref. [6] derived the critical current nodes B_n in the thin film limit. The B_z periodicity for the critical current oscillation, in the limit of large magnetic field, is $\Delta B_\infty = 1.842\Phi_0/L^2$. Refs. [6, 8] showed that in the thin film junction, the nodes B_n are not evenly spaced. In our device, the lithographically defined dimension is $L = 1.5\mu$m, thus ΔB_∞ should equal 1.88 mT. The $\Delta B_n = B_{n+1} - B_n$ extracted from our measurement in Fig. 1b is given in the table 1. The normalized $\Delta B_n/\Delta B_\infty$ values are close to the theoretical values in Ref. [6].

units	ΔB_0	ΔB_1	ΔB_2
mT	1.48	1.76	1.78
Normalized	0.79	0.94	0.95
Theory [6]	0.8173	0.9866	0.9946

Supplementary Table 1. Spacing between the I_c nodes $\Delta B_n = B_{n+1} - B_n$. Upper table, first line is in units of mT, second line is normalized by ΔB_∞. Lower table shows theoretical values from Ref. [6].

We note that in most of the literature, a simplified model is used to estimate the periodicity of the Fraunhofer map. It assumes magnetic field penetration through an area $A = LW' = L(W + 2\lambda_L)$, where λ_L is the London penetration length. So the magnetic field periodicity is $\Delta B_{\text{sim}} A = \Phi_0$. This applies to JJs made with bulk superconductors ($\lambda_L \gg L$). Translating this to the the thin film SC limit, we get an effective area $A_{\text{eff}} = L^2/1.842$, and $W'_{\text{eff}} = L/1.842$. Supplementary Fig. 5 shows the size of the JV in the y-direction agrees with this W'_{eff}.

ii. Extracting the ϕ_{bias} in Fig. 2d

In Fig. 2b-c, the measurement is taken by subtracting the I_{bias} case by the zero bias case. To extract the effective phase difference between SC electrodes ϕ_{bias}, the experimental results are fit to the following equation,

$$j_y(x) = J_c \cdot [\sin(\phi_e(x, B_z) + \phi_{\text{bias}}) - \sin(\phi_e(x, B_z))] \tag{10}$$

Here J_c (critical current density) and ϕ_{bias} are the two fitting parameters, while $L = 1.5\ \mu$m, $B_z = B_{\text{z,ext}} = 0.95$ mT are fixed parameters. The fitting results at each I_{bias} are shown in Supplementary Fig. 3.

iii. Extracting the ϕ_{eff} in Fig. 2h

In Fig. 2f-g, the measurement is taken by subtracting the I_{bias} case by the $-I_{\text{bias}}$ case. The ϕ_{eff} shown in Fig. 2h is $\phi_{\text{eff}} = \frac{16 B_{\text{eff}} L^2}{\pi^2 \Phi_0}$. The external magnetic field induced phase is $\phi_{\text{ext}} = \frac{16 B_z L^2}{\pi^2 \Phi_0}$. The experimental results are fit to the following equation,

$$\begin{aligned} j_y(x) &= J_c \cdot [\sin(\phi_e(x, B_z) + \phi_{\text{bias}}) - \sin(\phi_e(x, B_z) - \phi_{\text{bias}})] \\ &= 2 J_c \sin\phi_{\text{bias}} \cdot \cos[\phi_e(x, B_{\text{eff}})] \\ &\equiv J_0 \cdot \cos[\phi_e(x, B_{\text{eff}})] \end{aligned} \tag{11}$$

Here J_0 and B_{eff} are the fitting parameters, $L = 1.5\ \mu$m is fixed. The fitting results are shown in Supplementary Fig. 4f-j.

In both cases of fitting ϕ_{bias} and ϕ_{eff}, the portions of the reconstructed $j_y(x)$ with the distance to the edge of the SC smaller than the NV stand-off distance are excluded from the fitting process, to avoid the ringing and distortion effects of the reconstructed result near the edge.

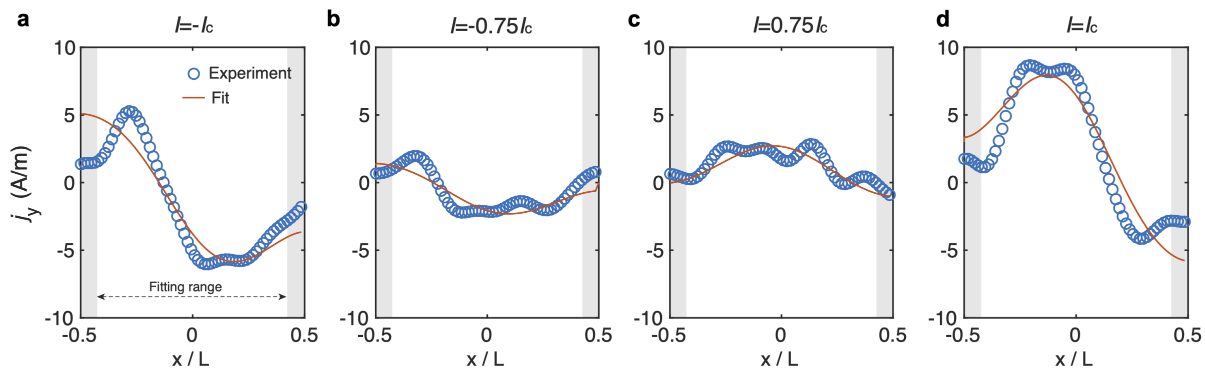

Supplementary Figure 3. **Extracting SC phase difference ϕ_{bias} from current profile measured at different I_{bias}.** Current flow profile at the center of the JJ measured using the finite to zero bias current sequence, as described in Fig. 2b-c in the main text. The grey areas which corresponds to regions closer to the JJ edge by the stand-off distance of the NV (≈180 nm), are excluded from the fitting. The bias current in each panel is **(a)** $-I_c$, **(b)** $-0.75 \cdot I_c$, **(c)** $0.75 \cdot I_c$ and **(d)** I_c. The blue circles represent the reconstructed j_y at the junction, and the red lines represent the fit using sinusoidal current-phase relation and ϕ_{bias} as fitting parameter. The extracted ϕ_{bias} is shown in Fig. 2d in the main text.

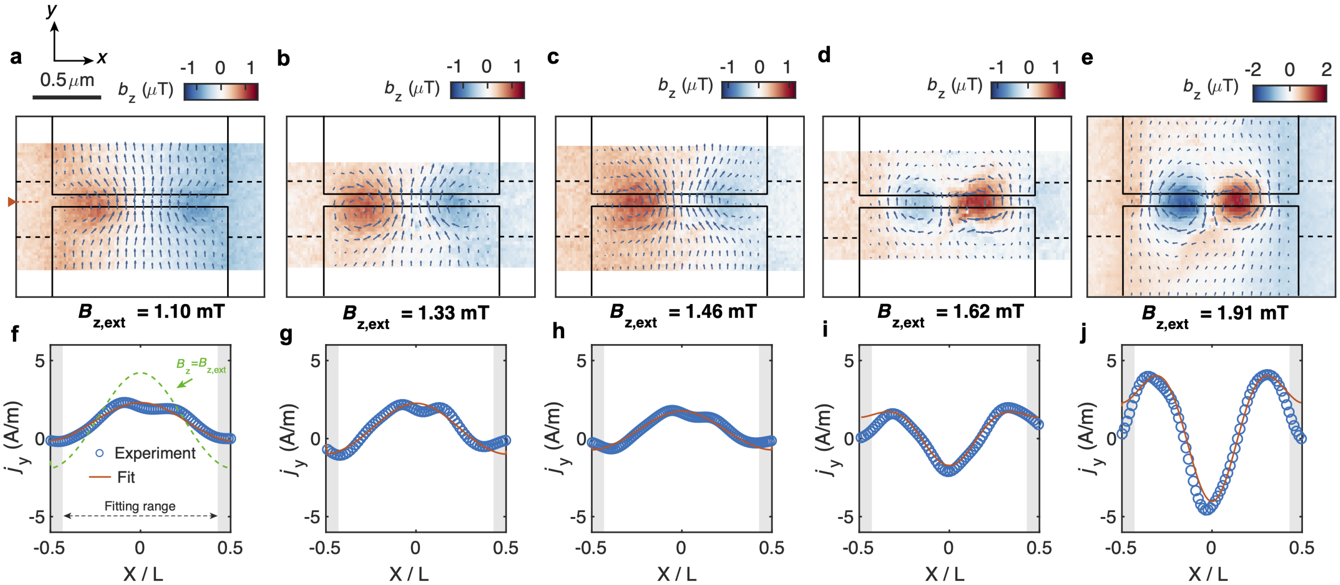

Supplementary Figure 4. **Josephson current flow at various magnetic flux around** $B_z = B_0$**. a-e,** show the spatial maps of current flow and z-direction magnetic field measured using symmetric $\pm I_{\rm bias}$ sequence as Fig. 2f-g in the main text, at external field values as shown by the labels above. **(a)-(c)** are $B_z < B_0$ and 0-JV; **(d)-(e)** are $B_z > B_0$ and 1-JV. The Josephson current flow switches sign from 0- to 1-JV. **(a)** and **(e)** are the same as Fig. 2f and g in the main text. The bias current used during the measurement in **(a)** $I_{\rm bias}/I_c \approx 0.7$; **(b)** $I_{\rm bias}/I_c \approx 0.7$; **(c)** $I_{\rm bias}/I_c \approx 0.9$; **(d)** $I_{\rm bias}/I_c \approx 0.6$; **(e)** $I_{\rm bias}/I_c \approx 0.8$. We emphasize again that the normalized shape of j_y is not expected to depend on $I_{\rm bias}/I_c$, as shown in Supplementary Fig. 5. So the result presented in the main text is insensitive to the exact value of $I_{\rm bias}/I_c$. **(f-j)** Circles show the reconstructed current flow at the center of JJ extracted from **(a)-(e)**, and the lines show the fitting to extract effective magnetic field $B_{z,\rm eff}$, as shown in Fig. 2h in the main text. The dashed green line in **(f)** shows that the $j_y(x)$ profile expected from the $\phi_{\rm ext}$ induced by the external field, which does not match our measurement. The red lines show the fitting results to extract $\phi_{\rm eff}$. The grey areas which corresponds to regions closer to the JJ edge by the stand-off distance of the NV (≈ 150 nm), are excluded from the fitting.

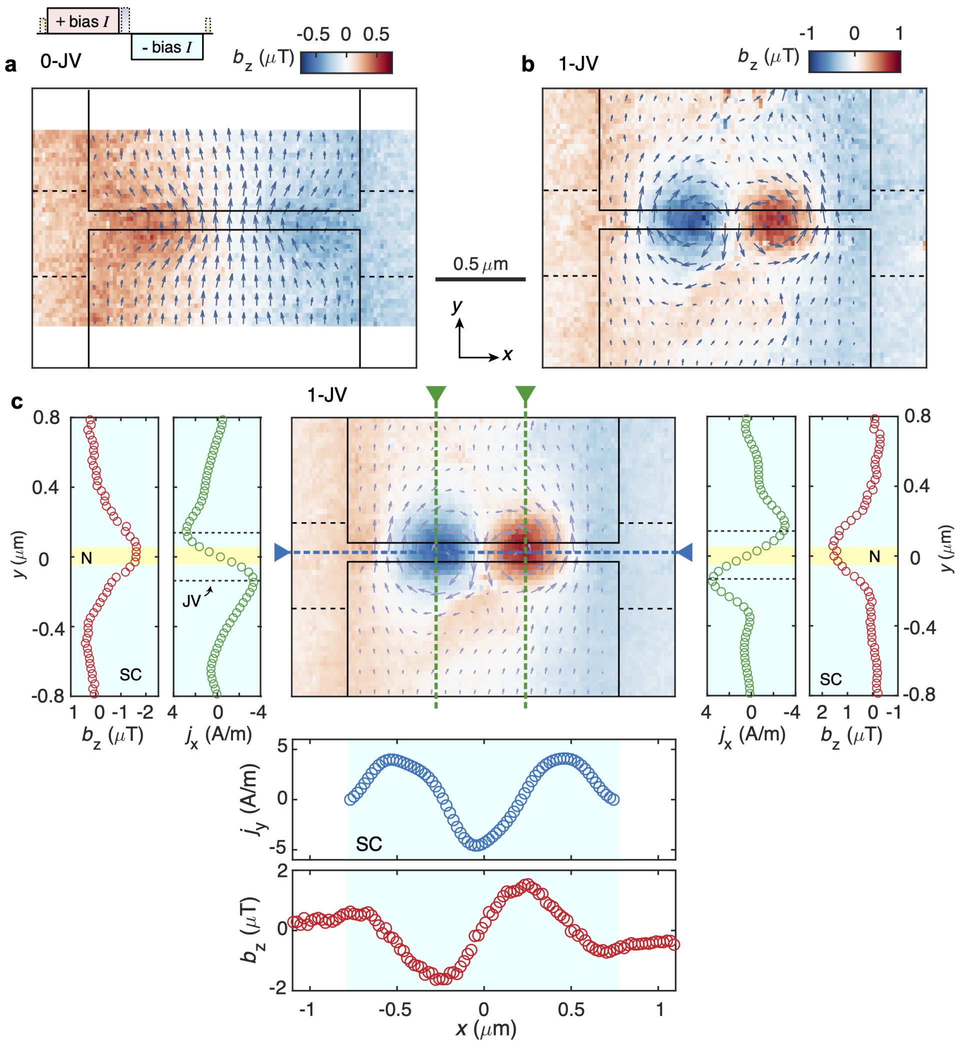

Supplementary Figure 5. **Additional measurements using symmetric bias $\pm I_{\text{bias}}$ sequence. a-b,** show spatial maps of current flow and z-direction magnetic field measured at the same external B_z as Fig. 2f-g in the main text, but using $I_{\text{bias}} = 0.5 I_c$ instead of I_c. Here we use colour scales with half the range, and the quiver with double the length per unit current density as in Fig. 2f-g. The shape of the current flow is almost the same, while the amplitude is half of those in Fig. 2f-g, as expected. The measurement is done at $T = 7$ K. **c,** shows the current flow and b_z line cut from Fig. 2g in the main text. The $j_x(y)$ line trace along the vertical direction shows the JV extends in to the SC electrodes by $\delta W \approx 350$ nm, making the effective area of the junction $A = LW'$, where $W' = W + 2\delta W \approx 850$ nm. This is consistent with the effective area $L^2/1.842$ as derived in Ref. [6].

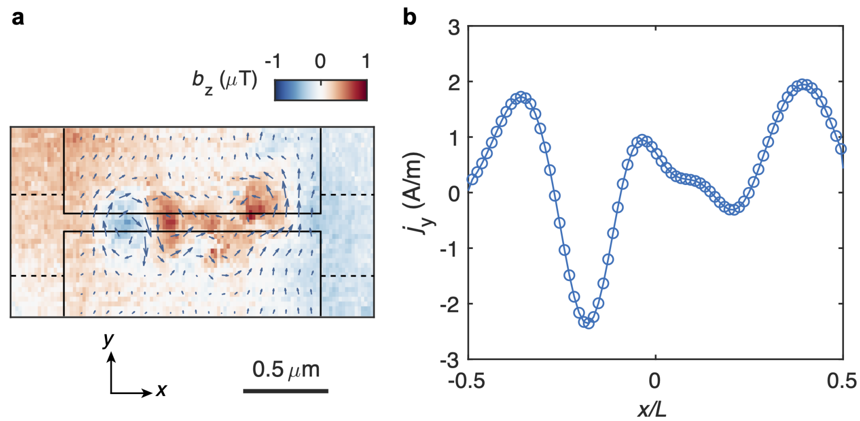

Supplementary Figure 6. **Current flow for 2-JV state. a,** Spatial maps of current flow and z-direction magnetic field measured using the symmetric $\pm I_{\text{bias}}$ sequence as Fig. 2f-g in the main text, measured at $B_z \approx 4$ mT and $T = 7$ K. **b,** Line cut of current flow at the center of the JJ showing cosine-like current profile with twice the oscillations as in Fig. 2g, indicating 2 JVs at the junction. The circles show the reconstructed current value, the line is a guide for the eye connecting the circles.

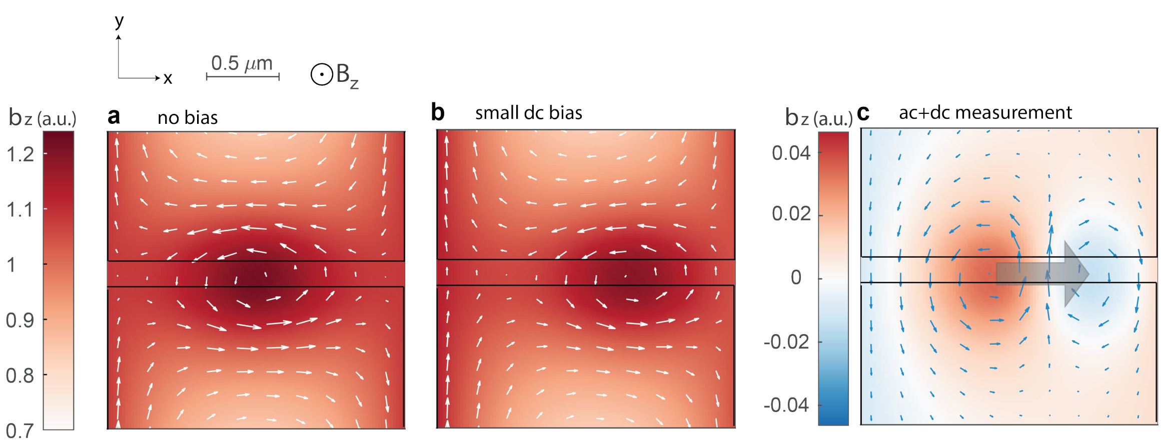

Supplementary Figure 7. **JV response to small changes in bias current. a-b,** Schematic drawings of current flow and and z-component of the magnetic field at two slightly different bias current, showing the position of JV controlled by the bias current. Colour scale is the same for both maps, in the unit of flux-quantum. **c,** The difference between **(a)** and **(b)** shows feature similar to Fig. 3d in the main text. As the bias current moves the JV along x-direction, the distance between the two current loops in **(c)** represents the size of the JV.

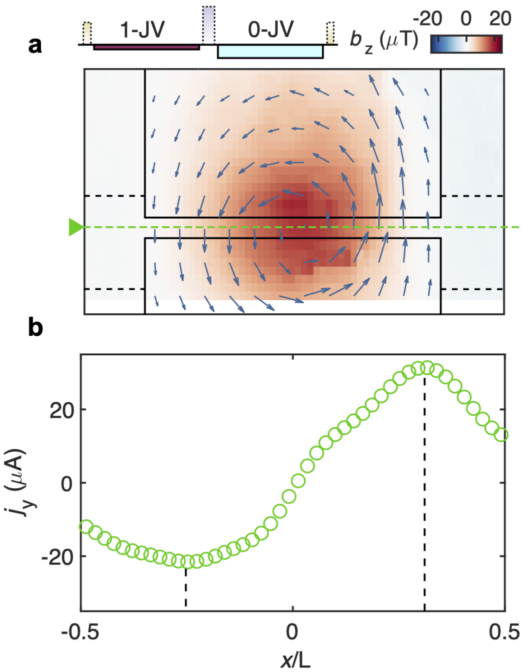

Supplementary Figure 8. **Lateral size of the JV. a,** Same map as Fig. 3f as the main text. The green dashed line indicate the position of the line cut shown in **(b)**. **b,** Line trace of j_y taken at the center of the JJ. The distance between the peak and valley of j_y indicates the lateral size of the JV. The size of the JV along x direction is about 500 nm. It is consistent with the distance between the center of the loops in Fig. 3e, which effectively measures $\partial b_z/\partial x$ of the JV (Supplementary Fig. 7). The measured JV size is slightly smaller than the theoretical size $\lambda_J \approx 780$ nm (see Methods), because the JV is constrained by L which is comparable to $2\lambda_J$.

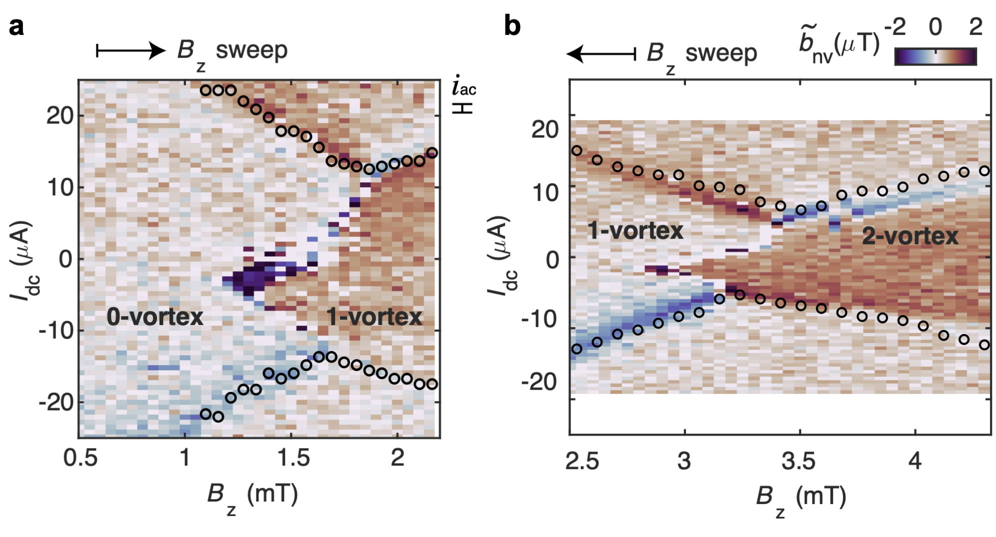

Supplementary Figure 9. **Additional measurements showing the competition between ground state configurations. a,** differential ac magnetic field measurement similar to Fig. 3b in the main text, when external B_z is swept from low to high field. The result shows the phase diagram is insensitive to B_z sweeping direction. **b,** differential ac magnetic field measurement at the range when 1- and 2-JV states overlap, showing the phase boundary below I_c extends only from the 2-JV state.

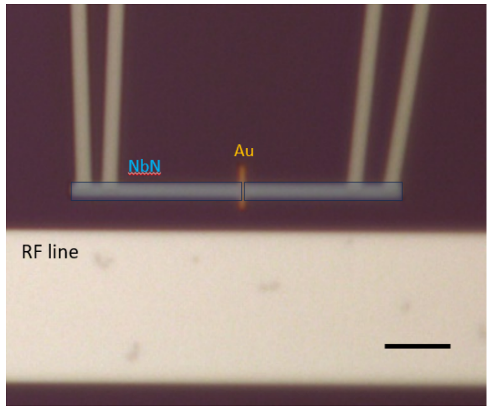

Supplementary Figure 10. **Optical image of the JJ device.** Optical micro-graph showing one of the JJ devices used in the paper. The SC electrodes made with NbN are false coloured. The RF line is used to deliver the microwave pulses to manipulate the NV. Scale bar is 5 μm.

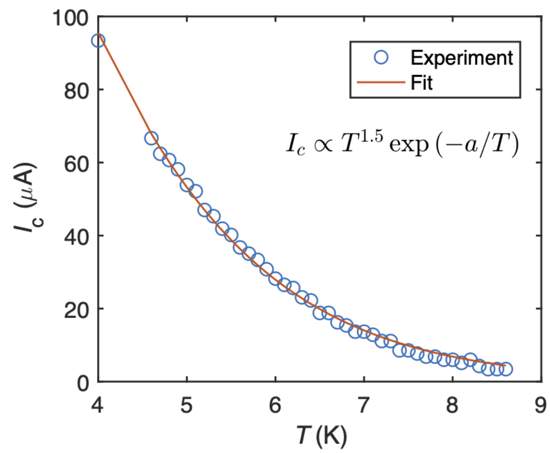

Supplementary Figure 11. **Temperature dependence of the critical current.** Temperature-dependent critical current at zero magnetic field versus fitted curve for a diffusive junction [9].

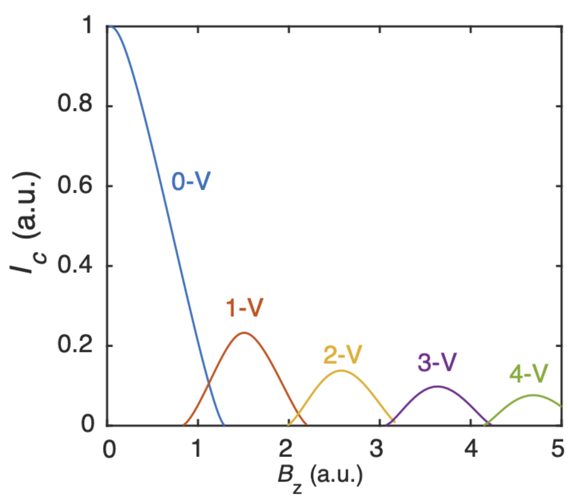

Supplementary Figure 12. **Overlapping ground state solutions in JJs with strong self field effect.** Analytical solutions of the non-linear sine-Gordon equation [10] showing critical current I_c for ground state configurations with different number of JVs, as indicated by the line traces of different colours. The traces are generated with junction length $L = 3\lambda_J$ to highlight the overlap regions.

Supplementary Note 5. DETAIL OF RECONSTRUCTING CURRENT FLOW FROM MAGNETIC FIELD

We show examples of this process with data taken for 0- and 1-JV states in Supplementary Fig. 13. Two NV centers with different axis were used when taking these data-sets, as indicated by the arrows in Supplementary Fig. 13a and e.

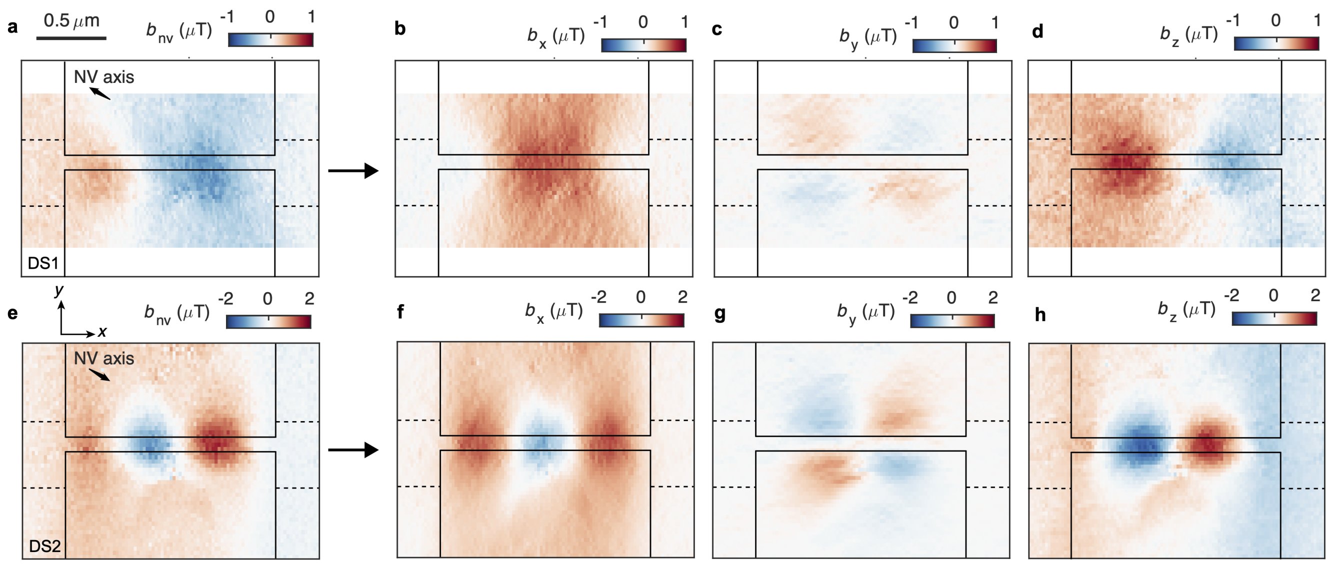

Supplementary Figure 13. **Examples of converting $b_{\rm nv}$ to $b_{x,y,z}$. a and e** show magnetic field projected along NV axis measured at two different external b_z, which we refer to as dataset1 (DS1) and dataset2 (DS2). **b-d,** show the vector magnetic field $b_{x,y,z}$ reconstructed from **(a)**. **f-h,** show the vector magnetic field $b_{x,y,z}$ reconstructed from **(e)**. DS1 is measured at external field $B_z = 1.46$ mT. DS2 is measured at external field $B_z = 1.91$ mT. The NV directions point partially out of plane, and their in-plane projections are shown in the insets of **(a)** and **(e)**. The scale bar is shared by all colour maps.

We employ the Fourier [11], regularization [12] and machine learning [13] methods to reconstruct the current flow. For the Fourier method, the full padded data is used in the current reconstruction. For the regularization and machine learning methods, the padded b_z is cut down to 2 times of the measurement window due to computational constraints. In the following, h is the stand-off distance of the NV sensor from the sample plane, and we first describe the methods and then show the results.

1. Fourier method [11]. The current and the in-plane components of the magnetic field are related in the Fourier space via

$$\begin{aligned} j_y(\mathbf{k}) &= b_x(\mathbf{k}, h) \cdot \frac{2}{\mu_0} e^{hk} \\ j_x(\mathbf{k}) &= -b_y(\mathbf{k}, h) \cdot \frac{2}{\mu_0} e^{hk} \end{aligned} \tag{12}$$

here μ_0 is the vacuum permeability. A low-pass Hanning filter $\mathcal{W}$ is applied to $j_{x,y}(\mathbf{k})$ before Fourier transforming back to the real space $j_{x,y}(x, y)$,

$$\mathcal{W} = \begin{cases} 0.5 \cdot [1 + \cos(k\alpha h/2)], & \text{for } k < 2\pi/\alpha h \\ 0, & \text{for } k < 2\pi/\alpha h \end{cases} \tag{13}$$

here α sets the cut-off wavelength in the reconstruction. The reconstructed current outside the device area is small and set to zero. We compare the effect of $\alpha \in [1, 2]$ in Supplementary Fig. 14. Although increasing α mitigates the ringing (spatial features oscillating faster than h), large α also smears out the result and reduces the amplitude of the reconstructed current. All of the results in the main text are reconstructed with $\alpha = 1.5$ to balance between these effects, but the conclusion about Josephson current induced phase in Fig. 2d and h from the main text does not rely on the choice of α.

2. Regularization method. For this method we follow Ref. [12] and the code there-in. Briefly speaking, it uses kernels K_1, K_2 that takes into account the finite thickness of the SC film $d = 35$ nm, and b_z is related to $j_{x,y}$ via

$$b_z(x, y, h) = K_1(x, y, h, d) * j_x(x, y) + K_2(x, y, h, d) * j_y(x, y) + N(x, y) \tag{14}$$

here * represents the convolution integral, $N(x, y)$ is noise. To reconstruct the current, the following regularization functional is minimized

$$\min(||K_1 * j_x + K_2 * j_y - b_z||^2 + \lambda(||\mathcal{L}j_x||^2 + ||\mathcal{L}j_y||^2) \tag{15}$$

here $\mathcal{L}$ is the Laplacian ∇^2, λ is the regularization parameter. Compared with the Fourier method, this functional penalizes fast oscillations in the reconstructed current flow. To account for the current flow outside the field-of-view, reflection rule at the boundaries is applied to the padded data. The results using regularization method is shown in Supplementary Fig. 15b, f.

3. Machine learning method. The neural network based reconstruction follows a similar construction to that performed in Ref. [13] with some modifications for reconstruction of current density. The magnetic field is passed to a fully connected neural network which has an output image $g(x, y)$. This is a stream function whose derivatives define the current density,

$$\nabla \times [g(x, y)\hat{z}] = \mathbf{j}(x, y) \tag{16}$$

which enforces the final current density to have zero divergence.

To encode the spatial resolution of the reconstructed current density, which is limited by the NV to sample standoff distance ($d_{\mathrm{nv}} = 150$ nm for DS1, $d_{\mathrm{nv}} = 130$ nm for DS2), we model each pixel as a Gaussian distribution with a width of $\sigma = d_{\mathrm{nv}}/2$. This acts to broaden the output stream function and remove fast oscillating terms before the derivatives are determined.

The calculated current densities are then transformed into a single magnetic field image that is compared with the original measured magnetic field, which forms the loss function, and the neural network weights are updated accordingly. The results using machine learning method is shown in Supplementary Fig. 15c, g.

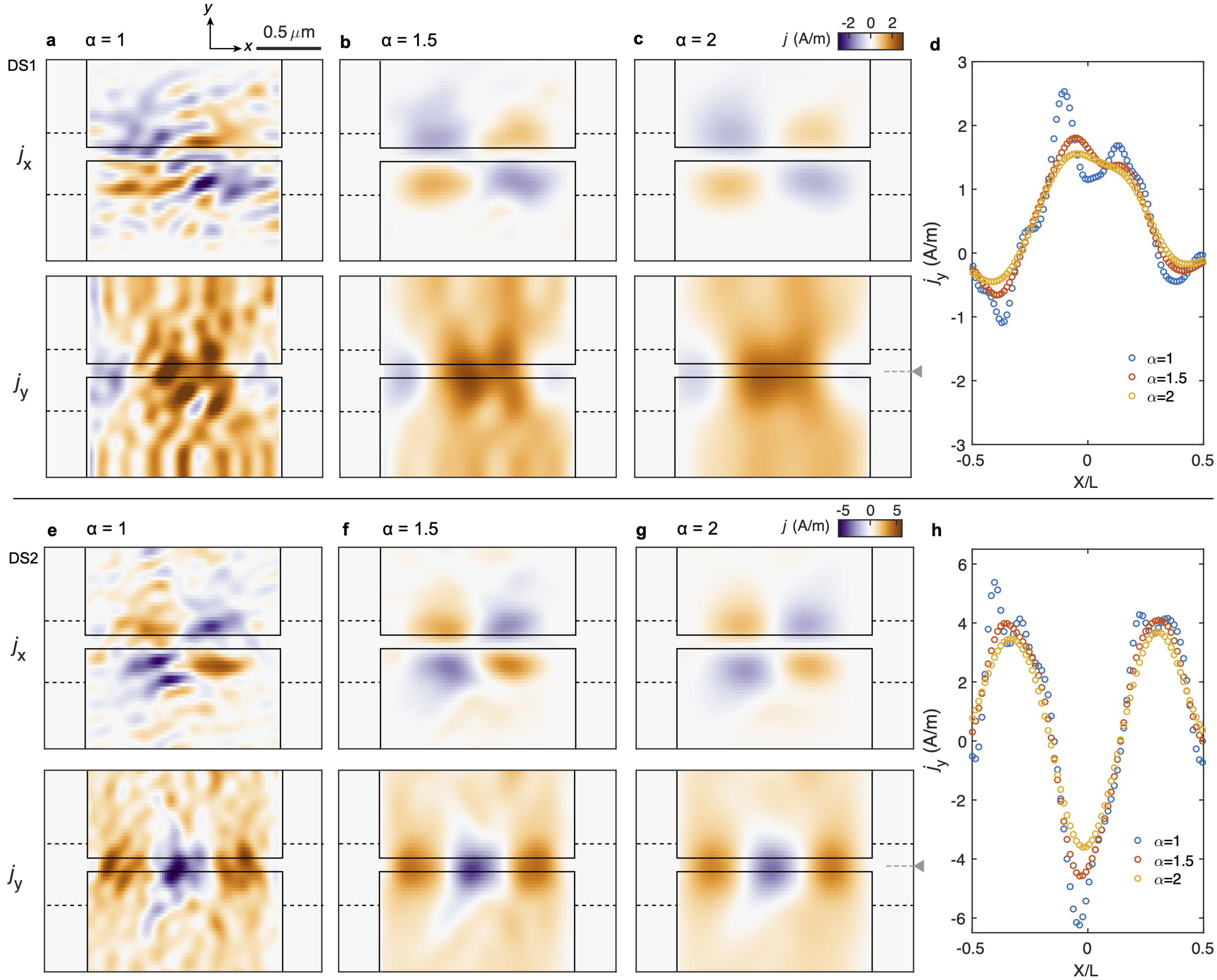

Supplementary Figure 14. **Comparison of current flow reconstructed from Fourier methods with different filter functions. a-c,** show the reconstructed current flow $j_{x,y}$ from DS1 using the Fourier method with cut-off parameter $\alpha =$ 1, 1.5, 2. **d,** show the line trace j_y with different α at the center of JJ, as indicated by the arrow in **(c)**. **e-h,** show the corresponding results for DS2. In both cases, increasing α mitigates ringing in the reconstructed current, but also reduces the amplitude of the current. So the results in the main text are reconstructed with $\alpha = 1.5$. The scale bar is shared by all colour maps.

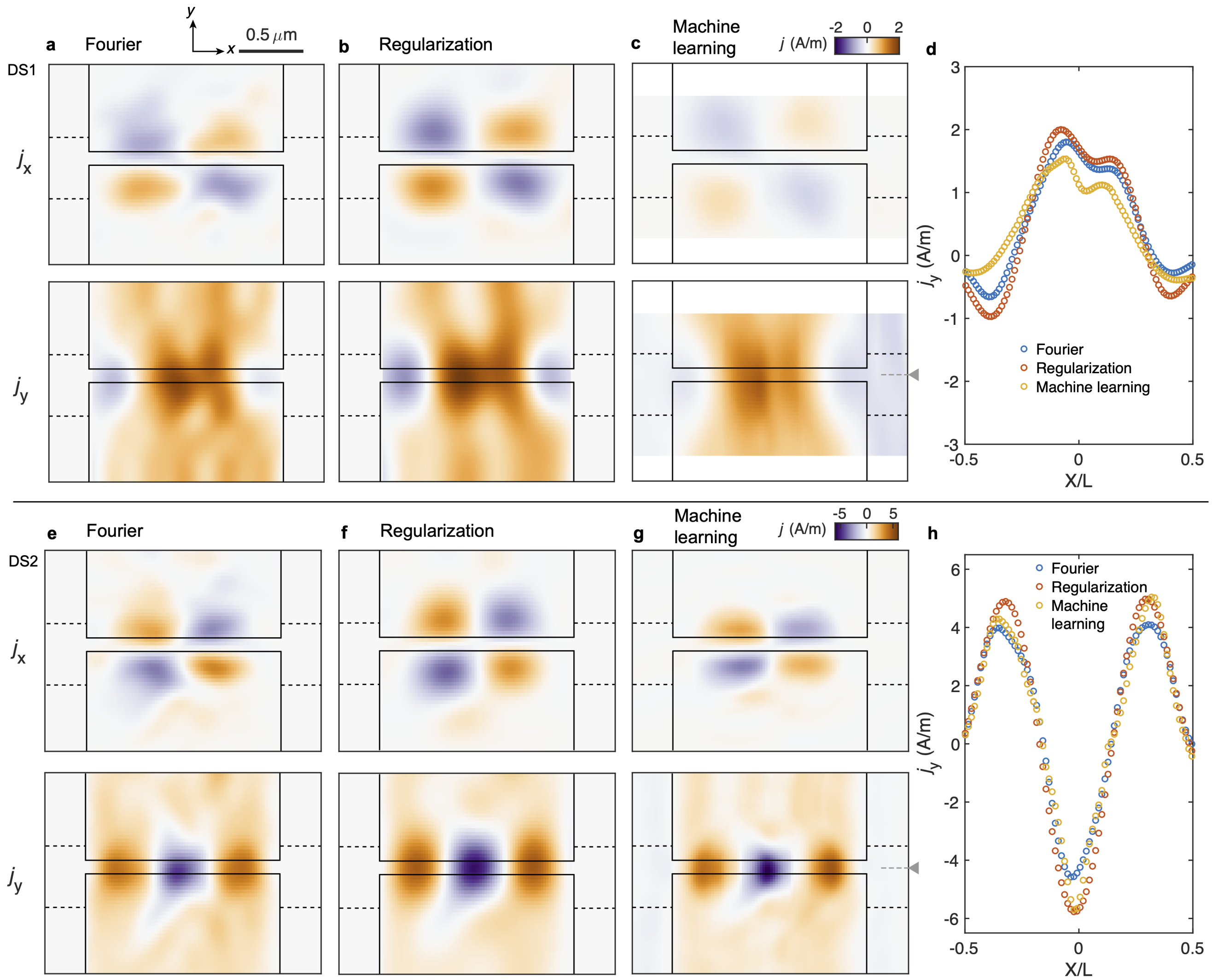

Supplementary Figure 15. **Comparison of current flow reconstructed from different methods. a-c,** show the reconstructed current flow $j_{x,y}$ from DS1 using the **(a)** Fourier ($\alpha = 1.5$), **(b)** regularization, and **(c)** machine learning methods. **d,** show the line trace j_y with different methods at the center of JJ, as indicated by the arrow in **(c)**. **e-h,** show the corresponding results for DS2. The scale bar is shared by all colour maps.

Supplementary Note 6. LACK OF DIODE EFFECT AT 7 K

In our experiment, the Josephson diode effect (JDE) is not observed when the current induced phase is not strong enough. Supplementary Fig. 16a shows the critical current I_c and related asymmetry parameter η at $T = 7$ K. Compared to the result in Fig. 4a, η vanishes to zero even for $B_z \neq 0$ (broken time-reversal symmetry).

From the local measurement of the current flow, we find broken inversion symmetry at $T = 7$ K. Using the sequence that measures the difference of symmetric $\pm I_{\mathrm{bias}}$ (Fig. 2f-g in the main text), the current profile $j_y(x)$ at the center of JJ is not symmetric with $x = 0$, suggesting the inversion symmetry breaking.

Supplementary Fig. 16c and d show two examples of $j_y(x)$. The measured $j_y(x)$ is fit with a non-uniform critical current profile. To the first order, the critical current density $J_c(x) = J_{c0}(p \cdot \frac{x}{L} + 1)$ (Supplementary Fig. 16b). $p > 0$ indicates larger critical current on the right side ($x > 0$). This leads to lower j_y minima for $x < 0$ in the 0-JV case, and higher j_y maxima for $x > 0$ in the 1-JV case. These features are qualitatively observed in all five data sets measured (Supplementary Fig. 4f-j).

Furthermore, we can quantitatively estimate the non-uniformity of the critical current. The measured current profile $j_y(x)$ is given by a modified version of Supplementary Eqn. 11,

$$j_y(x) = J_{c0}(p \cdot \frac{x}{L} + 1) \cdot [\sin(\phi_e(x, B_{\mathrm{eff}}) + \phi_{\mathrm{bias1}}) - \sin(\phi_e(x, B_{\mathrm{eff}}) + \phi_{\mathrm{bias2}})] \tag{17}$$

During the fitting, J_{c0}, p and B_{eff} are the fitting parameters. For given p and B_{eff}, we first find ϕ_{bias1} (ϕ_{bias2}) that corresponds to $+I_c$ ($-I_c$), and then use Supplementary Eqn. 17 to obtain $j_y(x)$. We note that although not all the data sets shown in Supplementary Fig. 4f-j are measured at $|I_{\mathrm{bias}}| = |I_c|$, the difference should be small. The junction length $L = 1.5\mu$m is fixed during the process.

The fitting results of slope p for all data sets are shown in Supplementary Fig. 16e. The linear $J_c(x)$ is just the first order correction, used as a toy model to highlight the non-uniform critical current density. In reality the critical current density could change along x direction due to variations of the SC/N interface transparency, separation W of the junction, etc. The fitting result in Supplementary Fig. 16e suggests $J_c(x > 0) > J_c(x < 0)$, consistent with the result from the current flow results measured at $T = 4$ K (Fig. 4). Overall, our local measurements show that inversion symmetry breaking at the JJ could be ubiquitous owing to extrinsic artefacts in the fabrication process, and may or may not manifest in the global measurement of asymmetric critical current.

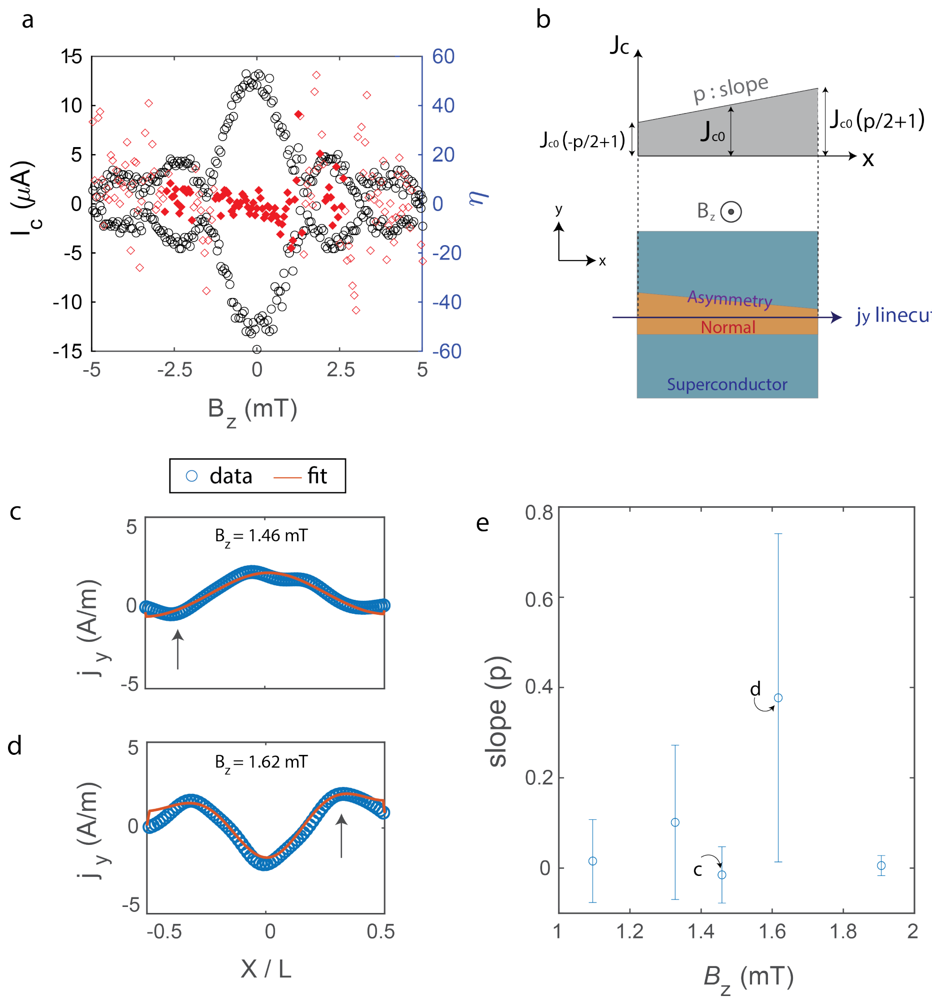

Supplementary Figure 16. **Critical current and inversion symmetry breaking at $T = 7$ K. a,** Critical current I_c and asymmetry factor $\eta = \frac{|I_c^+|-|I_c^-|}{|I_c^+|+|I_c^-|}$ versus perpendicular external magnetic field B_z. Compared with the $T = 4$ K result in Fig. 4a, η here averages to zero and JDE is negligible at T =7 K. The black circles show the critical current, the red diamonds show η. The η points where either of the $|I_c^{\pm}| < 3\mu$A is shown as unfilled diamonds, due to the large uncertainty arising from the small I_c. **b,** Upper panel shows the non-uniform critical current $J_c(x) = J_{c0}(p \cdot \frac{x}{L} + 1)$ used to fit the measured current profile in **(d)-(e)**. lower panel shows a schematic drawing showing of the inversion symmetry breaking at the junction, which could be caused by extrinsic factors such as non-uniform junction width. **c-d,** Circles show the measured current profile at $y = 0$ in the JJ measured with NV sequence as described in Fig. 2f-g in the main text, at **(c)** $B_{z,\mathrm{ext}} = 1.46$ mT (Supplementary Fig. 4h), **(d)** $B_{z,\mathrm{ext}} = 1.62$ mT (Supplementary Fig. 4i). Lines are fitting results using the non-uniform $J_c(x)$ as shown in **(b)**. Arrows point at the extrema of current profile. The j_y minima is smaller at $x < 0$ for 0-JV, and the maxima is larger at $x > 0$ for 1-JV. **e,** Fitting result of the slope p at each B_z. All the results except $B_z = 1.91$ mT show $p > 0$, indicating larger J_c for $x > 0$.

Supplementary Note 7. JOSEPHSON DIODE EFFECT ARISING FROM SYMMETRY BREAKING AND JOSEPHSON CURRENT INDUCED PHASE

In this section we examine the roles of time-reversal and inversion symmetry, and current flow induced phase in realizing the JDE as explained in Fig. 4 of the main text, using a model with two lumped JJs in parallel. From a phenomenological perspective, the minimum requirement for JDE is that the current phase relation contains more than just the first harmonic term, plus a phase offset, $I(\phi) = a_1 \sin(\phi) + a_2 \sin(2\phi + \phi_0)$ [14, 15]. The second harmonic term could be due to the ballistic transport in the JJ or high transparency of the SC/N interface, which are difficult to verify experimentally. Using a two-junction model, we show that broken time reversal and inversion symmetry, combined with the Josephson current induced phase can effectively cause such a second harmonic term in current phase relation, even when starting with only the first harmonic term for the diffusive and low-transparency JJ. A similar model was proposed in Refs. [16, 17], here we present more analysis in the context of the Josephson diode effect.

Supplementary Fig. 17a shows a schematic drawing of the two-junction model. The JJ studied in our paper could be regarded as a set of lumped JJs in parallel, so we consider the simplest case of two lumped JJs with critical current $J_{1,2}$. Inversion symmetry breaking is indicated by $J_1 \neq J_2$. The phase difference across the junction consists of the external magnetic field contribution f_{ext}, and the Josephson current induced phase f_{cip}. The total bias current across the junction is

$$I_{\text{bias}} = J_1 \sin(\Delta\phi - \frac{f_{\text{ext}} + f_{\text{cip}}}{2}) + J_2 \sin(\Delta\phi + \frac{f_{\text{ext}} + f_{\text{cip}}}{2}), \tag{18}$$

where $\Delta\phi \in [-\pi, \pi]$ is the phase difference between the SC electrodes. The Josephson current induced phase of the left and right junctions is

$$f_{\text{cip}} = \mathscr{L}_k \left[J_1 \sin(\Delta\phi - \frac{f_{\text{ext}} + f_{\text{cip}}}{2}) - J_2 \sin(\Delta\phi + \frac{f_{\text{ext}} + f_{\text{cip}}}{2}) \right], \tag{19}$$

where $\mathscr{L}_k$ is proportional to the kinetic inductance.

We discuss three representative scenarios.

1. Neglecting Josephson current induced phase. If $f_{\text{cip}} = 0$ in Supplementary Eqn. 18, the I_{bias} only contains the first harmonic term of $\Delta\phi$ with a phase offset, and JDE does not exist.

2. $J_1 = J_2$. Supplementary Eqn. 19 is reduced to $f_{\text{cip}} = -2\mathscr{L}_k \cos(\Delta\phi) \sin(f_{\text{ext}} + f_{\text{cip}})$, which yields the same solutions of f_{cip} when $\Delta\phi \leftrightarrow -\Delta\phi$. This means $I_{\text{bias}}(\Delta\phi) = -I_{\text{bias}}(-\Delta\phi)$, and JDE does not exist.

3. $J_1 \neq J_2$. In this case, f_{cip} needs to be solved numerically. Taking the limit of $f_{\text{cip}} \ll f_{\text{ext}}, \Delta\phi$, i.e., $\mathscr{L}_k J_i \ll 1$, we expand terms in Supplementary Eqn. 19 to first order of f_{cip}, and get

$$f_{\text{cip}} \simeq \mathscr{L}_k \left[J_1 \sin(\Delta\phi - \frac{f_{\text{ext}}}{2}) - J_2 \sin(\Delta\phi + \frac{f_{\text{ext}}}{2}) - \frac{f_{\text{cip}}}{2} \left[J_1 \cos(\Delta\phi - \frac{f_{\text{ext}}}{2}) + J_2 \cos(\Delta\phi + \frac{f_{\text{ext}}}{2}) \right] \right]. \tag{20}$$

   Combined with Supplementary Eqn. 18, we find

$$\begin{aligned} I_{\text{bias}} \simeq & J_1 \sin(\Delta\phi - \frac{f_{\text{ext}}}{2}) + J_2 \sin(\Delta\phi + \frac{f_{\text{ext}}}{2})) - \frac{f_{\text{cip}}}{2} \left[J_1 \cos(\Delta\phi - \frac{f_{\text{ext}}}{2}) - J_2 \cos(\Delta\phi + \frac{f_{\text{ext}}}{2}) \right] \\ = & J_1 \sin(\Delta\phi - \frac{f_{\text{ext}}}{2}) + J_2 \sin(\Delta\phi + \frac{f_{\text{ext}}}{2})) + \\ & \frac{\mathscr{L}_k}{2} \frac{J_1^2 \sin(2\Delta\phi - f_{\text{ext}}) + J_2^2 \sin(2\Delta\phi + f_{\text{ext}}) - 2J_1 J_2 \sin(2\Delta\phi)}{2 + \mathscr{L}_k \left[J_1 \cos(\Delta\phi - \frac{f_{\text{ext}}}{2}) + J_2 \cos(\Delta\phi + \frac{f_{\text{ext}}}{2}) \right]}. \end{aligned} \tag{21}$$

   Here the second harmonic term of $\Delta\phi$ with a phase shift is present, and JDE can be observed.

We also numerically solve for the critical current in the two-JJ model when the current flow induced phase is included. At each external magnetic flux f_{ext}, we first solve for f_{cip} at individual $\Delta\phi \in [-\pi, \pi]$ in Supplementary Eqn. 19. The (f_{cip}, $\Delta\phi$) is then plugged into Supplementary Eqn. 18 to find the maximum (minimum) I_{bias} as I_c^+ (I_c^-). Three cases of $J_{1(2)}$ are considered. When the system is inversion symmetric, i.e., $J_1 = J_2$, the current flow induced phase only lifts the node and does not manifest JDE (Supplementary Fig. 17d). When $J_1 \neq J_2$, $I_c^\pm$ becomes asymmetric when $f_{\text{ext}} \neq 0$. In particular, the JDE changes polarity when exchanging J_1 and J_2, or changing the sign of external field (Supplementary Fig. 17b and c). The critical current nodes are near half-integer of Φ_0 because of the two lumped JJs in the model (effectively a SQUID), but it does not affect the interpretation.

We note that the above result also applies to the case with strong self field effect, by replacing the kinetic inductance with the geometric inductance of the junction, and replacing the f_{cip} with the phase induced by the current-generated magnetic field, as pointed out in Refs. [16, 18].

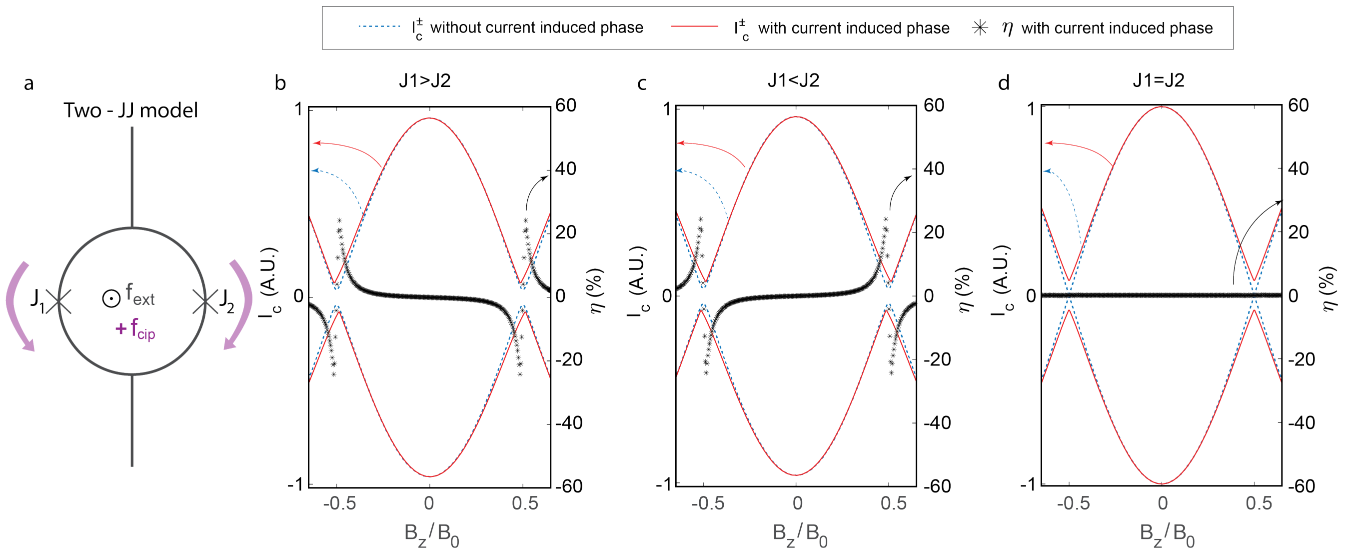

Supplementary Figure 17. **The two-junction model.** **a,** Schematics drawing of the model, showing left(right) JJs with critical current of $J_{1(2)}$ forming a loop. The total phase difference between the JJs comes from the external magnetic field f_{ext}, and the Josephson current induced phase f_{cip}. **b-d,** Numerical simulation of forward/backward critical current $I_c^{\pm}$, and asymmetric parameter $\eta = \frac{|I_c^+|-|I_c^-|}{|I_c^+|+|I_c^-|}$ as a function of external flux when **(b)** $J_1 > J_2$, **(c)** $J_1 < J_2$ and **(d)** $J_1 = J_2$. In **(b)** and **(c)**, the difference between $J_{1,2}$ is 10 %. Red (Blue) lines show the critical current I_c calculated with (without) the current induced phase. Black stars show asymmetric factor η when the current flow induced phase is included. In the inversion symmetric case **(d)**, there is no diode effect. In the inversion symmetry broken cases $J_1 \neq J_2$ in **(b)** and **(c)**, the diode effect is present when the current induced phase is included. η changes sign for J_1 larger or smaller than J_2.

The JDE has garnered much attention due to its application in low dissipation electronics [14, 15, 19–24], and some of the more recent interest has focused on the connection between JDE and finite momentum pairing of the Cooper pairs in the JJ [14, 15, 22]. Here in our work we are able to pinpoint the origin of the observed JDE with a combination of measurements of electrical transport, and visualization of the current flow. The inversion symmetry breaking in our device likely arises from the non-uniform junction width or transparency ubiquitous in the nano-fabrication process. The Josephson current induced phase is revealed thanks to the local current flow mapping, because the JJ is not deep in the so-called "strong-junction" regime by the conventional metric. In our device $L \approx 2\lambda_J$ even at $T = 4$ K, and the calculation of λ_J depends on an estimate of λ_L which could vary from sample to sample. In this spirit, we summarize some additional ways to realize the JDE experimentally from the literature.

1. Trapped vortices in superconductors. The JDE requires breaking time reversal symmetry. This could come from the Abrikosov vortices (AV) trapped in thin film superconductors even after external magnetic field is retracted. When an AV is near the JJ, it causes a phase gradient along the transverse direction that mimics the effect of magnetic flux induced by external field [25]. In the case of layered SC, JVs could be trapped between layers due to history of an in-plane magnetic field [26]. Additionally, the trapped vortices could be caused by magnetic materials at the JJ or nearby [27].

2. Asymmetric injection of bias current. The inversion symmetry of the JJ could be broken by non-uniform critical current density. This could be due to local defects as mentioned above, or local temperature gradient [28]. The effect could be further enhanced by engineering electrodes to intentionally inject the current asymmetrically to the JJ [25].

3. Multi-layer SC. When multiple kinds of SC with different critical current is used, or in the case of heterogeneous film quality along the normal direction, JDE could develop when an in-plane external field perpendicular to the

junction is applied [29]. The mechanism is similar to the one described in our main text, for a JJ that exists in the yz plane and the external field is B_x.

Supplementary Note 8. TIME-DEPENDENT GINZBURG LANDAU SIMULATION

The total Ginzburg Landau (GL) free energy for a thin film S structure with thickness t_{SC}, under external magnetic field $B_{\mathrm{z,ext}}$, in SI unit, is,

$$F_{\mathrm{GL}} = t_{SC} \cdot \int d^2\mathbf{r} \left[-\alpha\eta(\mathbf{r})|\Psi|^2 + \frac{\beta}{2}|\Psi|^4 + \frac{1}{4m_e}|(-i\hbar\nabla - 2e\mathbf{A})\Psi|^2 \right] + \frac{1}{2\mu_0} \int d^3\mathbf{r} |\nabla \times \mathbf{A} - B_{\mathrm{z,ext}}|^2, \tag{22}$$

where m_e is the electron mass, e is the electron charge, μ_0 is the vacuum permeability, $\eta(\boldsymbol{r})$ is the inhomogeneity factor; $\eta = 1$ for the SC electrodes, and $\eta < 0$ for the normal area of the junction. For the strong junction simulations shown in Figs. 3 and 4, we use $\eta = -1$ for the normal region. The characteristic lengths here are the GL penetration length $\lambda = \sqrt{\frac{m_e\beta}{2\mu_0 e^2|\alpha|}}$ and the GL coherence length $\xi = \sqrt{\frac{\hbar^2}{4m_e|\alpha|}}$. For $\Psi = |\Psi|e^{i\theta}$, the super current density is $\mathbf{J} = \frac{e}{m_e}(\hbar\nabla\theta - 2e\mathbf{A})|\Psi|^2$, and the sheet current density is $\mathbf{K} = t_{SC}\mathbf{J}$.

In thermal equilibrium, with no bias current, the functions $\mathbf{A}(\mathbf{r})$ and $\Psi(\mathbf{r})$ should be chosen to minimize F_{GL}, subject to suitable boundary conditions. Minimizing with respect to Ψ leads to the Ginzburg-Landau differential equation for Ψ in the vector potential $\mathbf{A}$, and minimizing with respect to $\mathbf{A}$ produces a vector potential resulting from the applied magnetic field and from the supercurrent associated with the wave function Ψ.

If the vector potential $\mathbf{A}(\mathbf{r})$ is specified, the wave function Ψ can be obtained using a two-dimensional time-dependent Ginzburg-Landau equation, which will cause Ψ to relax at long times to at least a local minimum of F_{GL} in the given vector potential. We use the package in Ref. [30] to carry out the TDGL simulations for the junction, based on equations derived for dirty superconductors in Ref. [31]. Briefly speaking, the package solves the following dimensionless TDGL equation,

$$\frac{u}{\sqrt{1+\gamma^2|\Psi|^2}} \left(\frac{\partial}{\partial t} + i\mu + \frac{\gamma^2}{2}\frac{\partial|\Psi|^2}{\partial t} \right) \Psi = (\eta - |\Psi|^2)\Psi + (\nabla - i\mathbf{A})^2\Psi. \tag{23}$$

Here t is time; $u \approx 5.79$, $\gamma = 10$ are constants; $\mu(\mathbf{r}, t)$ is the electric potential. The variables Ψ, $\mathbf{A}$, μ and t in Supplementary Eqn. 23 are in dimensionless units given in Ref. [30]. The electric potential evolution results from the current continuity equation, where the total current $\mathbf{J}$ comprises of the super current and normal current,

$$\nabla \cdot \mathbf{J} = \nabla \cdot \mathrm{Im}[\Psi^*(\nabla - i\mathbf{A})\Psi] - \nabla^2\mu = 0. \tag{24}$$

On the SC/vacuum interface, the Neumann boundary conditions are used:

$$\begin{aligned} \hat{\boldsymbol{n}} \cdot (\nabla - i\mathbf{A})\Psi &= 0 \\ \hat{\boldsymbol{n}} \cdot \nabla\mu &= 0, \end{aligned} \tag{25}$$

where $\hat{\boldsymbol{n}}$ is the unit vector normal to the interface. On the interfaces between SC and current terminals (which is used to apply the bias current), Dirichlet boundary conditions on Ψ and Neumann boundary condition on μ are used,

$$\begin{aligned} \Psi &= 0 \\ \hat{\boldsymbol{n}} \cdot \nabla\mu &= |\boldsymbol{K}_{\mathrm{bias}}|, \end{aligned} \tag{26}$$

where $|\boldsymbol{K}_{\mathrm{bias}}| = I_{\mathrm{bias}}/L$. In the case where $I_{\mathrm{bias}} = 0$, the solution gives a chemical potential μ that is independent of position, leading to an equilibrium solution, where the supercurrent is divergence-free. When $I_{\mathrm{bias}} \neq 0$, provided that the total current is less than the critical current in the specified magnetic field, there will be a solution where the normal current decays rapidly near the normal contact, while μ is essentially a constant and the Ginzburg-Landau equation applies away from the contacts.

Ideally, the vector potential should be determined self-consistently with the computed wave function Ψ. This can be done using an iterative procedure, which will be described below. However, the iteration is computationally expensive, and the correction due to the self field is small in the thin-film limit. Consequently, the self field has been ignored in most of our calculations, and the vector potential was set by $B_{\mathrm{z,ext}}$ via $\nabla \times \mathbf{A} = B_{\mathrm{z,ext}}$.

-Simulation parameters

The results in Fig. 3c and Fig. 4e, f are simulated without the self field. A schematic drawing of the simulated device is shown in Supplementary Fig. 18a and the parameters used are

λ	400 nm
ξ	100 nm
L	1.5 μm
W_1	160 nm
W_2	140 nm
t_{SC}	35 nm

Supplementary Table 2. Parameters used in the TDGL simulation.

Here we choose $\lambda = \lambda_L$, the London penetration length measured by the experiment (Supplementary Fig. 1), ξ is chosen to realize similar critical current at zero magnetic field as the experiment at $T = 4$ K,when $\eta = -1$ in the normal region, and $W_{1,2}$ are chosen to reproduce the asymmetric features in the experiment. The total length in y direction of the simulated device is $Y = 7.5$ μm, with the current terminals attached along the edges of $y = \pm Y/2$. The maximum grid edge size is 40 nm. Below the critical current, a steady state solution can be found such that $\frac{\partial \Psi}{\partial t} = 0$. Above the critical current, a steady state cannot be found due to JV motion (ac Josephson effect), and is beyond the scope of this work.

-Simulation results

Below we describe how the results in the main text are obtained.

1. **Overlapping 0- and 1-JV states.** The overlapping JV states are generated using different initial conditions; the initial condition for the 0-JV states is a uniform and real Ψ (Supplementary Fig. 18b); the initial condition for the 1-JV state is a seed solution from the non-overlap part of the 1-JV state (Supplementary Fig. 18c). In the overlap area, the results is either 0- or 1-JV states depending on the initial condition; outside the overlap area, the results is independent of the initial condition. In other words, there are two local energy minima with respect to the spatial configuration of Ψ in the overlap region; and only one local minimum outside the overlap region. Under such a scenario the expectation from thermodynamics is hysteresis in the overlap region, with respect to the direction of the B_z or I_{bias} sweep. However, as we pointed out in the main text, this was not observed in the experiment and an open question for future work.

   The total Gibbs free energy shown in Fig. 3c is $\varepsilon = F_{GL} - I_{\text{bias}}\Phi_0\frac{\phi}{2\pi}$ to account for the bias current. Here ϕ is the mean value of $\theta(x)|_{y=y_0} - \theta(x)|_{y=-y_0}$ averaged over x. The result shown in Supplementary Fig. 18b-c is taken at $y_0 = 0.5\mu$m and insensitive to $y_0 \gg W_{1,2}$.

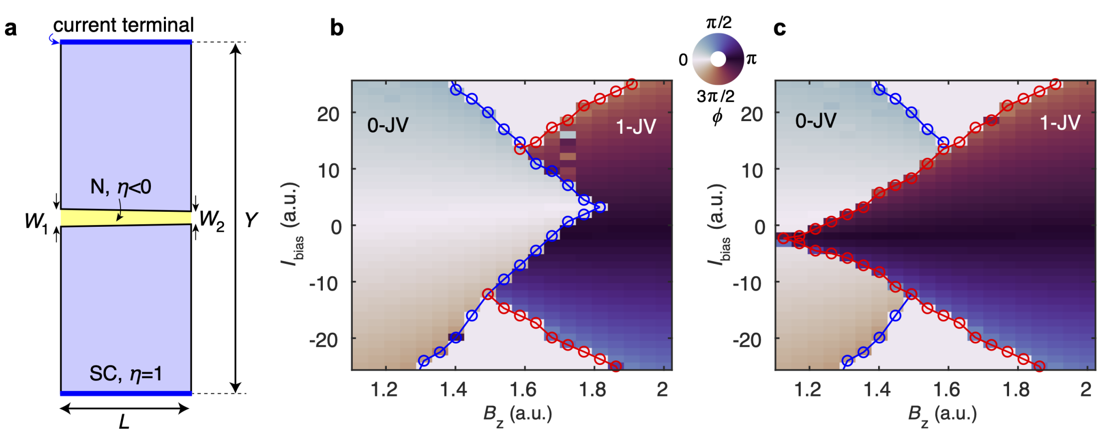

Supplementary Figure 18. **TDGL Simulation schematic and initial conditions**. **a,** Schematic drawing of the simulated device. The drawing is not to scale so as to highlight the junction area in the middle of the device. **b-c,** Phase difference across the junction the **(b)**0-JV and **(c)**1-JV state. The circles mark the critical current for the two solutions. The result beyond the critical current is blanked for clarity.

2. **Varying the critical current.** The critical current of the JJ is tuned by η of the normal region. For smaller critical current, such as the case at $T = 7$ K, $\eta = -5$. The current induced phase is enhanced when critical current is large ($\eta = -1$). Specifically, in the 0-JV state the transverse current near the JJ, J_x is reduced by the amount of the current flowing across the JJ; in the 1-JV state, however, J_x is enhanced by the vortical current (Supplementary Fig. 19). The phase difference $\phi(x)$ along the JJ in ref. [6] was derived when neglecting the Josephson current across the junction. The change of J_x when including the effect of the Josephson current leads to the current flow induced phase discussed in the main text.

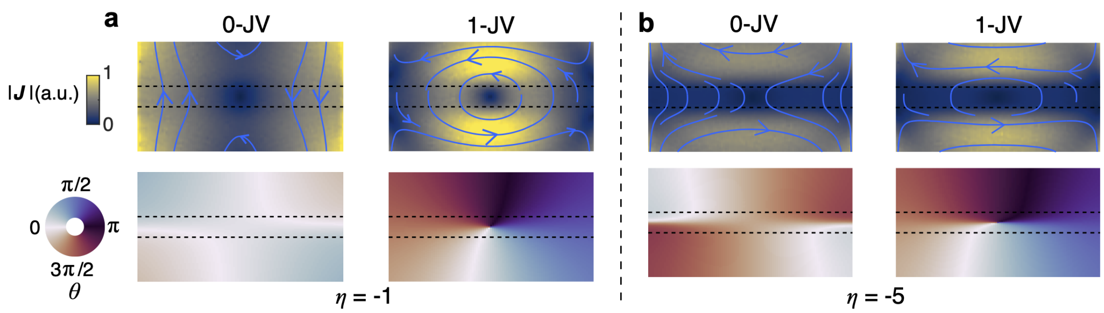

Supplementary Figure 19. **Varying critical current with η of the normal region**. **a-b,** Simulated local current density and superconducting phase using **(a)** $\eta = -1$ and **(b)** $\eta = -5$ for the normal area of the junction. The simulations here are done in a symmetric junction for clarity, with $W_1 = W_2 = 150$ nm. All cases are simulated at the same external magnetic field, at zero bias and neglecting self-field effect.

3. **Effect of coupling to the self-field.** We have investigated the self-field effect in the case $I_{\text{bias}} = 0$, by correctly including the self-generated magnetic field in the vector potential felt by the superconductor. The full vector potential can be written as $\mathbf{A} = \mathbf{A}_{\text{ext}} + \mathbf{a}$, where

$$\mathbf{a}(\mathbf{r}) = \frac{\mu_0}{4\pi} \int \frac{\mathbf{K}}{(\mathbf{r}')} |\mathbf{r} - \mathbf{r}'| d^2\mathbf{r}', \tag{27}$$

and $\mathbf{k}$ is the sheet current obtained by solving the Ginzburg-Landau equation in the presence of the vector potential $\mathbf{A}$. As an initial step, we find a first order correction $\mathbf{a}_0$ by substituting for $\mathbf{k}$ in (27) with the sheet current $\mathbf{k}_0$ obtained for $\mathbf{A} = \mathbf{A}_{\text{ext}}$. We then solve the Ginzburg-Landau equation with $\mathbf{A} = \mathbf{A}_{\text{ext}} + \mathbf{a}_0$, calculate a new value of $\mathbf{k}$, and iterate until convergence is reached.

We find that the 3D magnetic field energy (last term in Supplementary Eqn. 22) is larger for the 0-JV than the 1-JV state inside the overlap region. However, the total energy difference between the 0- and 1-JV states $\Delta\varepsilon = \varepsilon_0 - \varepsilon_1$ decreases when the self field effect is included. The fact that larger field energy results in lower total energy can be understood by the following argument. If one constrains Ψ to have the form $\Psi_0(\mathbf{r})$ calculated with $\mathbf{A} = \mathbf{A}_{\text{ext}}$ and substitutes it in Supplementary Eqn. 22, one finds

$$F_{\text{GL}} = F_{A_{\text{ext}}} - \int d^2\mathbf{r}\,\mathbf{k}_0 \cdot \mathbf{a} + \frac{1}{2\mu_0} \int d^3\mathbf{r}\,|\nabla \times \mathbf{a}|^2 + t_{SC}\frac{e^2}{m_e} \int d^2\mathbf{r}\,|\mathbf{a}|^2 |\Psi|^2. \tag{28}$$

For a thin film SC, the second and third terms scale with t_{SC}^2, while the last term scales with t_{SC}^3 and can be neglected. If we then choose $\mathbf{a}$ to minimize Supplementary Eqn. 28, we find $\mathbf{a}$=$\mathbf{a}_0$, and the second term on the right-hand side of Supplementary Eqn. 28 is -2 times the third term. This gives us the approximation

$$F_{\text{GL}} \approx F_{A_{\text{ext}}} - \frac{1}{2\mu_0} \int d^3\mathbf{r}\,|\nabla \times \mathbf{a}_0|^2. \tag{29}$$

This implies that coupling to the self field decreases the total energy by the amount of the 3D magnetic field energy, thereby favoring the 0-JV state over the 1-JV state.

A more complete calculation would allow for deviations of Ψ from the starting form Ψ_0, which will further reduce the total free energy. We do not have a simple expression for this effect, but it seems reasonable to assume that the reduction will also be greater when the induced magnetic field is greater. Moreover, we expect that the change in Ψ should be proportional to $\mathbf{a}_0$, and the resulting change in the free energy will be of relative order

$|\mathbf{a}_0|^2$. From our numerical calculations, we find that the approximation (Supplementary Eqn. 29) gives about twice of the total reduction in energy arising from the self-field coupling. The result is seen in Supplementary Fig. 20a-b.

In order to further confirm this analysis, we have performed numerical simulations where we have artificially strengthened the coupling to the magnetic field by decreasing λ while holding fixed the parameters ξ, m_e and α. As the superfluid density is proportional to λ^{-2}, we expect the magnetic field energy to scale as λ^{-4} while the energy without the self-field effect ($F_{\mathrm{A_{ext}}}$) scales as λ^{-2}. The results, plotted in Supplementary Fig. 20c, f, are in accord with this expectation. Finally, coupling to the self-field decreases the energy for the 0-JV state more than the 1-JV state (Supplementary Fig. 20d-f). This could be viewed as a result of the 0-JV state having larger magnetic field energy than the 1-JV state.

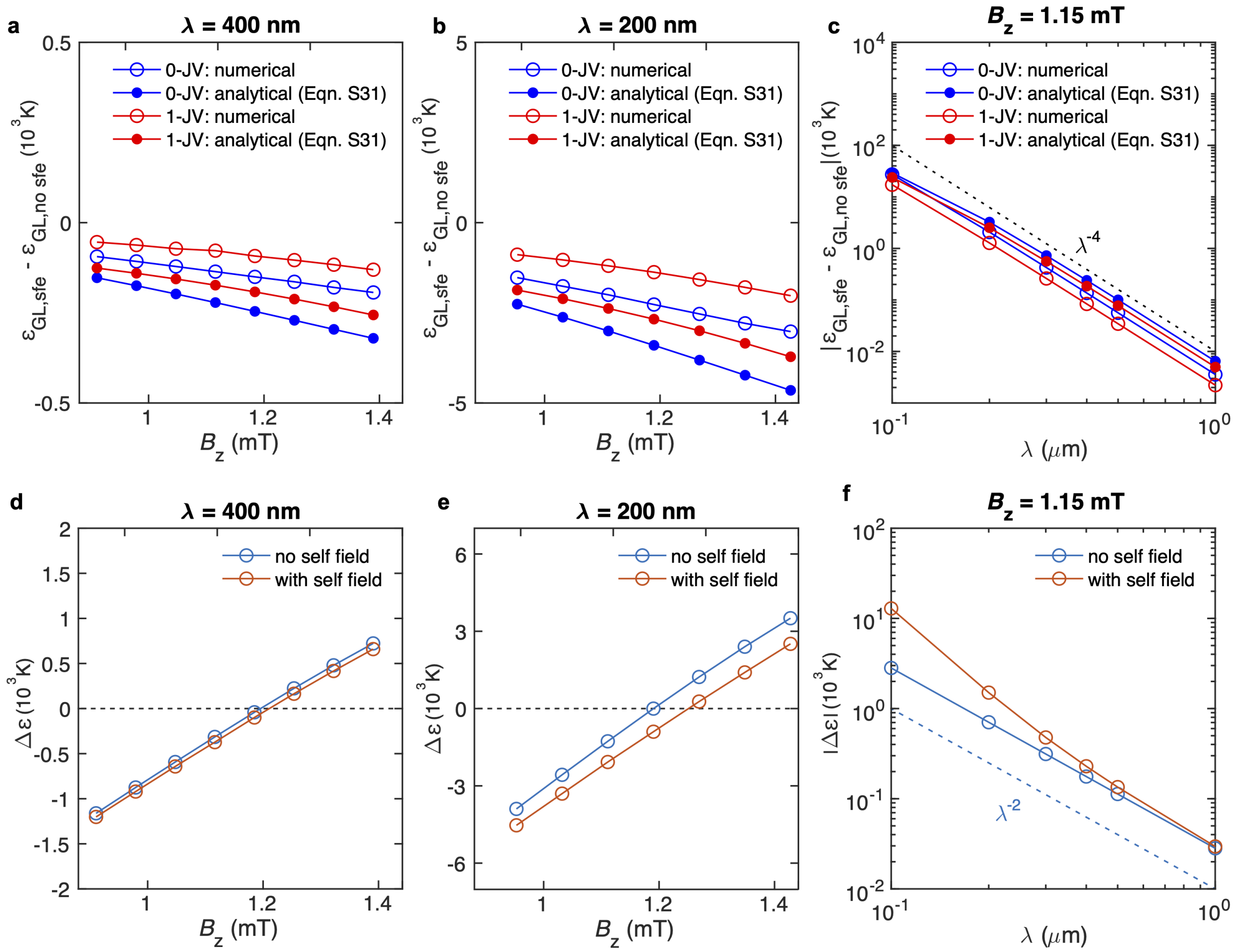

Supplementary Figure 20. **Energy difference including the self-field effect**. **a-b,** The energy difference of solutions with or without coupling to the self field, versus external magnetic field B_z. Results are taken at **(a)** $\lambda = 400$ nm, and **(b)** $\lambda = 200$ nm. The blue (red) colour points represent the 0- (1-) JV. The empty points are numerical results obtained by iterating both Ψ and $\mathbf{a}$. The filled points are results given by the approximate analytical formula Supplementary Eqn. 29, where the energy shift from coupling to the self field is the negative of the 3D magnetic field energy. **c,** Absolute value of the energy difference of solutions with or without coupling to the self-field, plotted versus of λ. In particular, in the analytical approximation given by Supplementary Eqn. 29, the energy difference is the magnetic field energy which is expected to scale with λ^{-4} (shown by the dashed line as a guide for the eye). **d-e,** Energy difference of the 0 and 1-JV states $\Delta\varepsilon = \varepsilon_0 - \varepsilon_1$ if the self field effect is included for **(d)** $\lambda = 400$ nm, and **(e)** $\lambda = 200$ nm. Smaller λ represents larger self field effect. **f,** $|\Delta\varepsilon|$ as a function of λ at fixed external magnetic field. The total energy difference between 0- and 1-JV states without coupling to the self-field is expected to scale with λ^{-2} (shown by the dashed line as a guide for the eye). Panels C and F are simulated at $B_z = 1.15$ mT. The simulations are done in a symmetric junction with $W_1 = W_2 = 150$ nm, and the external dc bias is zero.

Supplementary Note 9. SIMULATIONS FOR AN ASYMMETRIC GEOMETRY

We present in Supplementary Fig. 21 results of simulations comparing symmetric and asymmetric geometries.

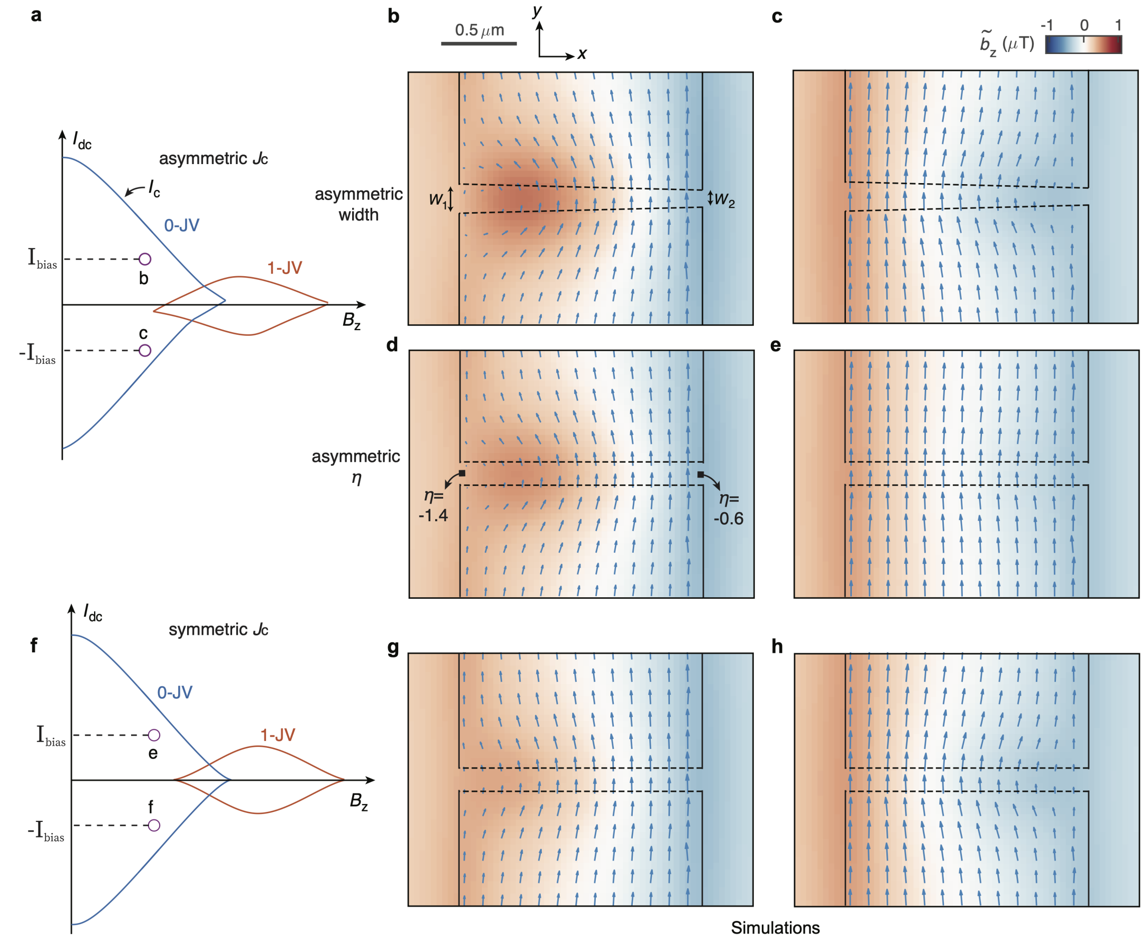

Supplementary Figure 21. **TDGL simulations on JJs with symmetric or asymmetric geometry.** **a, f,** Schematic drawing of critical current of 0- and 1-JV states versus external magnetic field B_z, for **(a)** inversion-asymmetric, and **(d)** inversion-symmetric junctions. **b-e,** Simulated current flow and z-direction of magnetic field from a differential measurement. The maps are taken in an asymmetric JJ with non-uniform critical current density along x direction. **(b)-(c)** are simulated with tilted junction width $W_1 > W_2$. **(d)-(e)** are simulated with non-uniform η factor in the normal region (η changes linearly with x from -1.4 to -0.6). The dc bias current are symmetric with zero as shown in **(a)**. **(b)-(c)** are the same as Fig. 4e-f in the main text. **g-h,** Simulated current flow and z-direction of magnetic field from a symmetric JJ with uniform critical current density along x direction. The dc bias current are shown in **(f)**. Current flow is inversion symmetric for $\pm I_{bias}$ when inversion symmetry of the JJ is preserved.

SUPPLEMENTARY REFERENCES

[1] Rohner, D. *et al.* Real-space probing of the local magnetic response of thin-film superconductors using single spin magnetometry. *Sensors* **18**, 3790 (2018).
[2] Ilin, K. *et al.* Critical current of Nb, NbN, and TaN thin-film bridges with and without geometrical nonuniformities in a magnetic field. *Phy. Rev. B* **89**, 184511 (2014).
[3] Charaev, I. *et al.* Proximity effect model of ultranarrow NbN strips. *Phys. Rev. B* **96**, 184517 (2017).
[4] Hu, R., Kerber, G. L., Luine, J., Ladizinsky, E. & Bulman, J. Sputter deposition conditions and penetration depth in nbn thin films. *IEEE Tran. on Appl. Superconductivity* **13**, 3288–3291 (2003).
[5] Kamlapure, A. *et al.* Measurement of magnetic penetration depth and superconducting energy gap in very thin epitaxial nbn films. *Appl. Phys. Lett.* **96**, 072509 (2010).
[6] Clem, J. R. Josephson junctions in thin and narrow rectangular superconducting strips. *Phys. Rev. B* **81**, 144515 (2010).
[7] Mints, R. & Papiashvili, I. Nonlocal electrodynamics of josephson junctions in thin films and fractional vortices. *Superconductor Sci. and Tech.* **15**, 307 (2002).
[8] Boris, A. A. *et al.* Evidence for nonlocal electrodynamics in planar josephson junctions. *Phys. Rev. Lett.* **111**, 117002 (2013).
[9] Dubos, P. *et al.* Josephson critical current in a long mesoscopic SNS junction. *Phys. Rev. B* **63**, 064502 (2001).
[10] Kuplevakhsky, S. & Glukhov, A. Exact analytical solution of the problem of current-carrying states of the josephson junction in external magnetic fields. *Phys. Rev. B* **76**, 174515 (2007).
[11] Roth, B. J., Sepulveda, N. G. & Wikswo Jr, J. P. Using a magnetometer to image a two-dimensional current distribution. *Journal of Appl. Phys.* **65**, 361–372 (1989).
[12] Meltzer, A. Y., Levin, E. & Zeldov, E. Direct reconstruction of two-dimensional currents in thin films from magnetic-field measurements. *Phys. Rev. App.* **8**, 064030 (2017).
[13] Dubois, A. *et al.* Untrained physically informed neural network for image reconstruction of magnetic field sources. *Phys. Rev. App.* **18**, 064076 (2022).
[14] Pal, B. *et al.* Josephson diode effect from cooper pair momentum in a topological semimetal. *Nat. Phys.* **18**, 1228–1233 (2022).
[15] Jeon, K.-R. *et al.* Zero-field polarity-reversible josephson supercurrent diodes enabled by a proximity-magnetized pt barrier. *Nat. Mat.* **21**, 1008–1013 (2022).
[16] Fulton, T., Dunkleberger, L. & Dynes, R. Quantum interference properties of double josephson junctions. *Phys. Rev. B* **6**, 855 (1972).
[17] Reinhardt, S. *et al.* Link between supercurrent diode and anomalous Josephson effect revealed by gate-controlled interferometry. *Nat. Comm.* **15**, 4413 (2024).
[18] Goldman, A. & Kreisman, P. Meissner effect and vortex penetration in josephson junctions. *Phys. Rev.* **164**, 544 (1967).
[19] Ando, F. *et al.* Observation of superconducting diode effect. *Nature* **584**, 373–376 (2020).
[20] Baumgartner, C. *et al.* Supercurrent rectification and magnetochiral effects in symmetric josephson junctions. *Nat. Nano.* **17**, 39–44 (2022).
[21] Wu, H. *et al.* The field-free josephson diode in a van der waals heterostructure. *Nature* **604**, 653–656 (2022).
[22] Lin, J.-X. *et al.* Zero-field superconducting diode effect in small-twist-angle trilayer graphene. *Nat. Phys.* **18**, 1221–1227 (2022).
[23] Hou, Y. *et al.* Ubiquitous superconducting diode effect in superconductor thin films. *Phys. Rev. Lett.* **131**, 027001 (2023).
[24] Nadeem, M., Fuhrer, M. S. & Wang, X. The superconducting diode effect. *Nature Reviews Physics* 1–20 (2023).
[25] Golod, T. & Krasnov, V. M. Demonstration of a superconducting diode-with-memory, operational at zero magnetic field with switchable nonreciprocity. *Nat. Comm.* **13**, 3658 (2022).
[26] Moler, K. A., Kirtley, J. R., Hinks, D., Li, T. & Xu, M. Images of interlayer Josephson vortices in $Tl_2Ba_2CuO_{6+\delta}$. *Science* **279**, 1193–1196 (1998).
[27] Gutfreund, A. *et al.* Direct observation of a superconducting vortex diode. *Nat. Comm.* **14**, 1630 (2023).
[28] Krasnov, V., Oboznov, V. & Pedersen, N. F. Fluxon dynamics in long josephson junctions in the presence of a temperature gradient or spatial nonuniformity. *Physical Review B* **55**, 14486 (1997).
[29] Sundaresh, A., Väyrynen, J. I., Lyanda-Geller, Y. & Rokhinson, L. P. Diamagnetic mechanism of critical current nonreciprocity in multilayered superconductors. *Nat. Comm.* **14**, 1628 (2023).
[30] Bishop-Van Horn, L. pytdgl: Time-dependent ginzburg-landau in python. *Comp. Phys. Comm.* 108799 (2023).
[31] Watts-Tobin, R. J., Krähenbühl, Y. & Kramer, L. Nonequilibrium theory of dirty, current-carrying superconductors: Phase-slip oscillators in narrow filaments near T_c. *Journal of Low Temp. Phys.* **42**, 459–501 (1981).